ABSTRACT

PULSED LASER ABLATION DEPOSITION AND OPTICAL CHARACTERIZATION OF HEXAGONAL-WURTZITE SILICON

by
Berzelius Ybanez Cada

Hexagonal-wurtzite silicon phase silicon is an unusual polymorph of silicon with potentially useful electro-optical properties. Previous studies using a simple deposition system demonstrated that laser ablation of the standard cubic-diamond silicon produces droplets containing hexagonal-wurtzite crystallites. In order to study the process parameters and to deposit larger hexagonal crystals, a new pulsed laser ablation system with variable parameters was assembled and tested. Deposition experiments were performed in high vacuum with different laser pulse power. Raman spectroscopy showed that the new system successfully produces hexagonal-wurtzite silicon. The droplet size distributions, measured with an optical microscope, were found to depend on the laser pulse power, target-substrate separation and the target rotation. The droplets of hexagonal crystallites varied in diameter from less than a micron to 49 micrometers. The deposited material was examined using scanning electron microscopy and optically characterized by white light transmission.

PULSED LASER ABLATION DEPOSITION AND OPTICAL CHARACTERIZATION OF HEXAGONAL-WURTZITE SILICON

by
Berzelius Ybanez Cada

A Thesis
Submitted to the Faculty of
New Jersey Institute of Technology
in Partial Fulfillment of the Requirements for the Degree of
Master of Science in Electrical Engineering

Department of Electrical and Computer Engineering

January 2004

APPROVAL PAGE

PULSED LASER ABLATION DEPOSITION AND OPTICAL CHARACTERIZATION OF HEXAGONAL-WURTZITE SILICON

Berzelius Ybanez Cada

Dr. Marek Sosnowski, Thesis Advisor — Date
Professor of Electrical and Computer Engineering, NJIT

Dr. Haim Grebel, Committee Member — Date
Professor of Electrical and Computer Engineering, NJIT

Dr. Zafar Iqbal, Committee Member — Date
Research Professor of Chemistry, NJIT

BIOGRAPHICAL SKETCH

Author: Berzelius Ybanez Cada

Degree: Master of Science

Date: January 2004

Undergraduate and Graduate Education:

- Master of Science in Electrical Engineering,
  New Jersey Institute of Technology, Newark, NJ, 2004

- Bachelor of Science in Chemical Engineering,
  New Jersey Institute of Technology, Newark, NJ, 2000

Major: Electrical Engineering

To my beloved family.

ACKNOWLEDGMENT

I would like to extend my deepest thanks to my advisor, Dr. Marek Sosnowski, for giving me the opportunity to work on this research project and for his patience and understanding. His guidance and encouragement were invaluable. Special thanks to Dr. Haim Grebel for his supervision, advisement, and support. I would also like to Dr. Haim Grebel and Dr. Zafar Iqbal for serving on my thesis committee and reviewing my thesis.

My fellow students and researchers in the Optical Waveguide Laboratory and the Ion Beam and Thin Film Research Laboratory deserve recognition for their assistance. Wenwen Luo deserves thanks for providing her expertise in SEM. I would like to thank Dr. Leszek Gladczuk in particular for his support and insight. Dr. Aidong Lan is also deserving of thanks for his help and training. Hui Han and Dr. Yan Zhang have also been very helpful.

Without the love and support of my parents Beethoven A. and Salud Y. Cada, I would never have come this far. They have always patiently supported my choices and I am very grateful for that.

The encouragement and support of my extended family and friends has been greatly appreciated.

I would like to thank Michele L. Kung for her love, encouragement, and support. Proofreading her thesis greatly improved my efficiency in formatting my own.

TABLE OF CONTENTS

TABLE OF CONTENTS
(continued)

Chapter **Page**

LIST OF TABLES

Table **Page**

LIST OF FIGURES

Figure **Page**

LIST OF FIGURES
(continued)

Figure **Page**

LIST OF FIGURES
(continued)

Figure **Page**

LIST OF FIGURES
(continued)

Figure **Page**

CHAPTER 1

INTRODUCTION

1.1 Objective

The objective of this thesis was to determine the pulsed laser ablation process parameters necessary to deposit the largest possible droplets of silicon in hexagonal wurtzite phase. Larger droplets are desirable for measuring the optical and electronic properties of the crystallites present in a droplet. The laser ablation system previously used in the optical waveguide laboratory lacked the flexibility to vary process parameters, therefore a new system was assembled to replace it.

1.2 Background Information

Silicon can exist in many different crystallographic phases. The standard phase used in fabrication of silicon wafers is the cubic-diamond lattice, which has a lattice constant of 0.543nm. This phase does not exhibit any useful optical properties. Once the particle size is reduced to the nanometer scale (nanocluster or nc-Si), silicon begins to exhibit optical properties such as photoluminescence and electroluminescence. A light emitting diode has even been made from nc-Si [1]. Nanometer scale Si can be manufactured by a number of methods such as ion implantation [2], plasma enhanced chemical vapor deposition [3], magnetron sputtering [4], thermal annealing of SiN_x films [5], and laser ablation.

Hexagonal silicon with lattice constants a=0.38 nm c=0.628 nm [6, 7] is one of the unusual phases of Si that can be created at high pressure and temperatures. For example, the ambient pressure cubic-diamond phase undergoes a nonmetal to metal

transition at 10-13 GPa to form a β-tin structure, which transforms on slow pressure release to a rhombohedral phase. The rhombohedral phase transforms reversibly at a pressure of 2 GPa to a body-centered-cubic phase labeled bc8. Heating the bc8 phase to above 200°C yields hexagonal-wurtzite silicon. Shear stresses at twin intersections of cubic-diamond silicon or a nonhydrostatic stress of 8 GPa in indentation experiments also form hexagonal-wurtzite silicon [8].

Si formed by laser ablation in the Optical Waveguide Laboratory at the New Jersey Institute Of Technology has been found by X-ray diffraction and Raman spectroscopy to be of a hexagonal-wurtzite structure regardless of substrate [8, 9]. Droplets of hexagonal Si in films grown at NJIT's Optical Waveguide Laboratory by PLA have shown a crystal orientation of <111> regardless of substrate [9, 10].

Measurements of hexagonal silicon in the optical waveguide laboratory have shown very large non-linear optical coefficients [11]. One would like to find out whether the large non-linear values stem from the existence of closed packed nanocrystallites or from larger crystals observed in the deposited material. With a greater understanding of hexagonal silicon's properties, useful non-linear, nano-optical materials may be realized [9]. It may be possible to eventually use hexagonal Si to construct optical switching devices.

1.3 Pulsed Laser Ablation

Pulsed laser ablation (PLA) is a deposition process in which a high intensity pulsed laser vaporizes a small area on the surface of a target. The vapor (ablated material) deposits on a substrate under controlled conditions (such as temperature and pressure), forming a thin

film. The film may be induced to grow on top of a crystal substrate with the same structure and very close lattice dimensions. It can be known as epitaxial growth.

PLA is a cold-wall process which excites only a small area of the target material in the focus of the incident light beam. Under vacuum, PLA is capable of maintaining purity in processing ambient. Purity is important because advanced functional devices are extremely sensitive to impurities. PLA also has excellent features from the viewpoints of safety and compatibility with the environment.

CHAPTER 2

LASER ABLATION SYSTEM

The laser ablation system assembled for this research consists of a vacuum chamber and a Lamda Physik 20 W KrF excimer laser (model EMG102) emitting ultraviolet radiation at a wavelength of 248 nm with 3 W of average power, 8 ns pulse duration, and 1-40 Hz variable repetition rate. In addition to the laser, another optical heat source was added to heat the target for this research, which will be discussed in Chapter 3. A schematic of the system is shown in Figure 2.1.

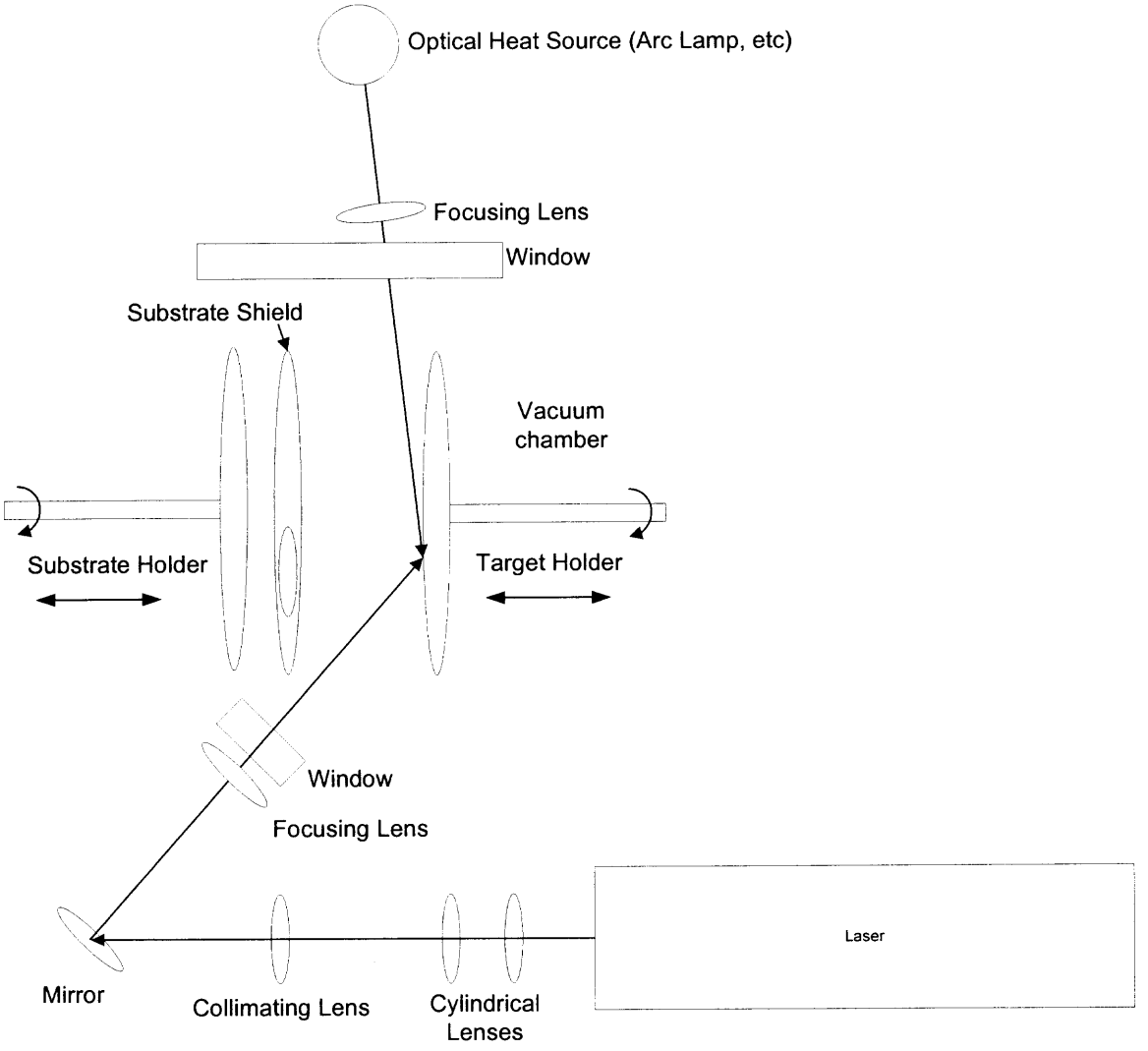

Figure 2.1 Laser ablation schematic.

The vacuum chamber is constructed of a modified stainless steel 10 cm six-way Con-Flat™ cross. A photograph of the chamber is shown in Figure 2.2. The left and right ports have large 10 cm diameter flanges sealed with Viton® O-rings and are used for target and substrate mounting respectively. A small angled port in the back (Figure 2.3) contains a window for the ultraviolet laser beam to pass through. Inside the chamber, a fused silica shield protects the laser window from being coated by laser ablated particles. Laser ablated particles would otherwise deposit on the window which is difficult to clean due to its geometry. The fused silica shield is transparent to ultraviolet light, inexpensive, and easy to remove, clean, and replace.

The large window in front is used for the optical heat source and for observation. The bottom port is connected to a stainless steel tee to which the turbomolecular pump, gate valve, and vacuum ionization gage are mounted. The top port flange is closed by a stainless steel blank, but it can easily be replaced to expand the capabilities of the system.

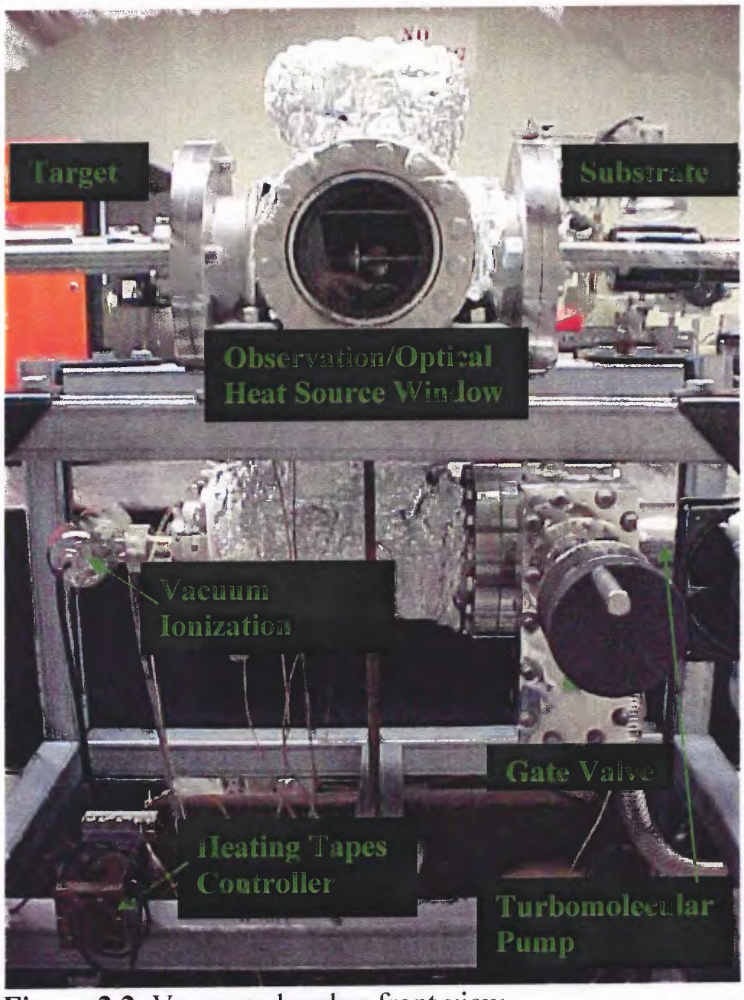

Figure 2.2 Vacuum chamber front view.

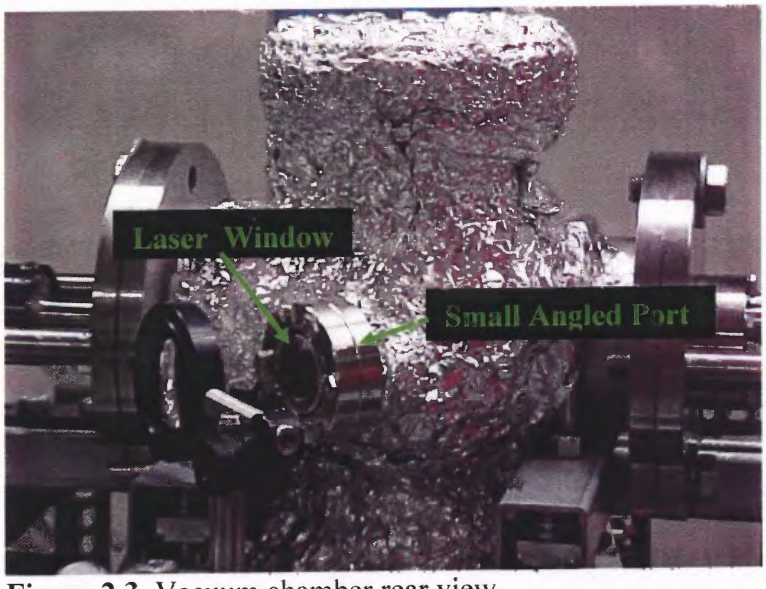

Figure 2.3 Vacuum chamber rear view.

The gate valve is closed when the chamber is open to atmosphere to protect the turbomolecular pump from contamination. To create the vacuum, the gate valve is opened first with the turbomolecular pump turned off. A mechanical pump shown in Figure 2.4 is then used to evacuate the chamber to a pressure of 10^{-3} Torr. Next, an air-cooled turbomolecular pump, shown in Figure 2.5, is turned on. It brings the base pressure down to the order of 10^{-6} Torr. The chamber is baked overnight under vacuum with heating tapes. This step helps outgassing of the chamber walls after the chamber has been exposed to the atmosphere. The heating tapes are connected to a controller which monitors the chamber temperature with a thermocouple. The controller prevents the chamber temperature from exceeding 110°C since some of the seals are Viton® rubber O-rings and would be damaged by excessive heat. Foil covers the tapes to help retain heat. After the chamber has cooled to room temperature, the pressure reaches ~10^{-7} Torr. A vacuum ionization gauge is used to measure the high vacuum achieved by the turbomolecular pump. To open the chamber to access the target and samples, the turbomolecular pump is turned off and allowed to wind down before turning off the mechanical pump. The chamber is then vented to the atmosphere by means of a valve on the turbomolecular pump.

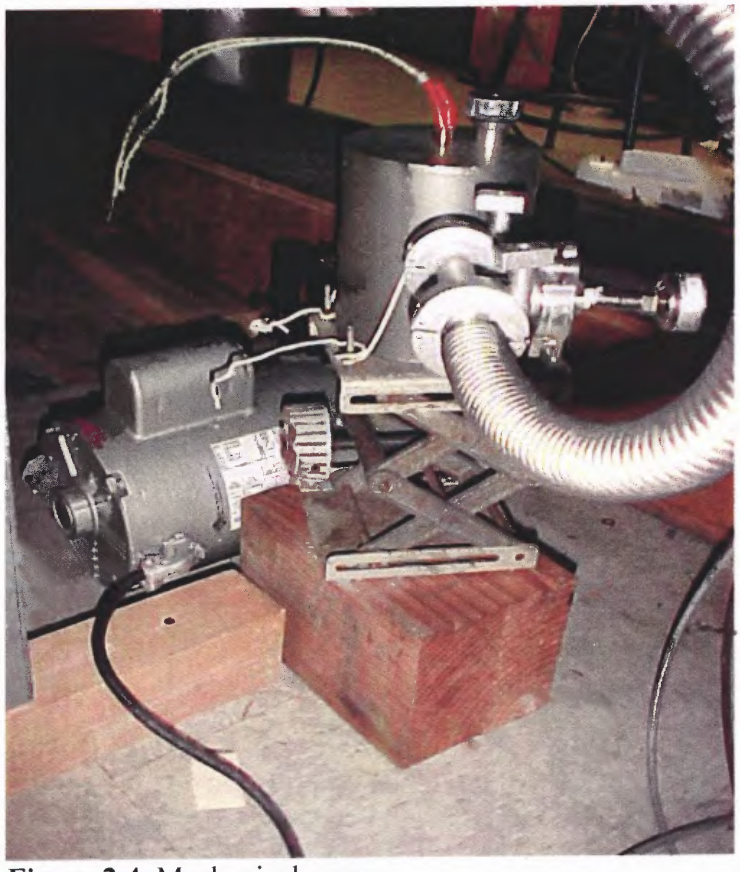

Figure 2.4 Mechanical pump.

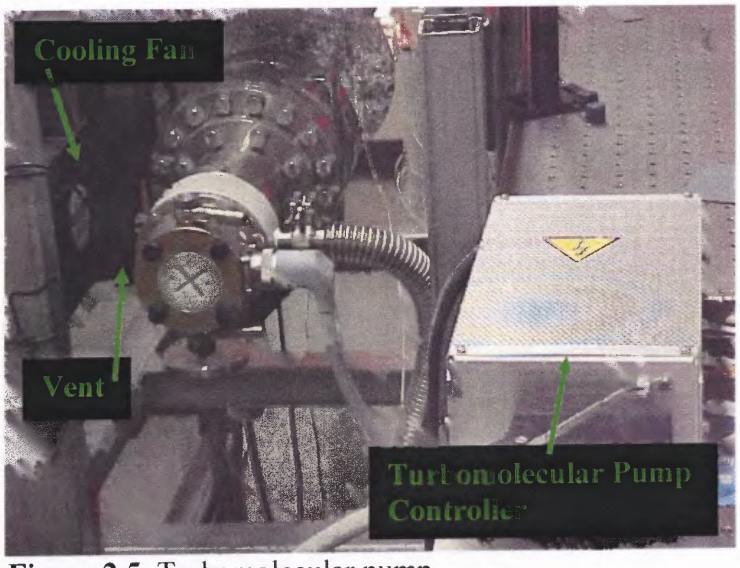

Figure 2.5 Turbomolecular pump.

The target used for this research is a silicon wafer 76.2 mm in diameter and 1 mm thick. It is <100> oriented, single-crystal cubic-diamond silicon (n-type, 10^{16} cm^{-3}). Low doping is desirable for deposited film purity. A relatively thick target was chosen so that deposition could be carried out longer before it became necessary to move the target to prevent the laser from drilling through it. During deposition, the target can be rotated by means of a rotary feedthrough which can be operated manually or with the attached motor. With the chamber at atmospheric pressure, the target holder (seen in Figures 2.6 and 2.7) can be moved towards and away from the substrate to adjust the target-substrate distance or to aid in aiming the laser. The rotational axis of the target can also be rotated, with the chamber at atmospheric pressure, about an axis offset from the center of the chamber shown in Figure 2.7 to create different traces on the target.

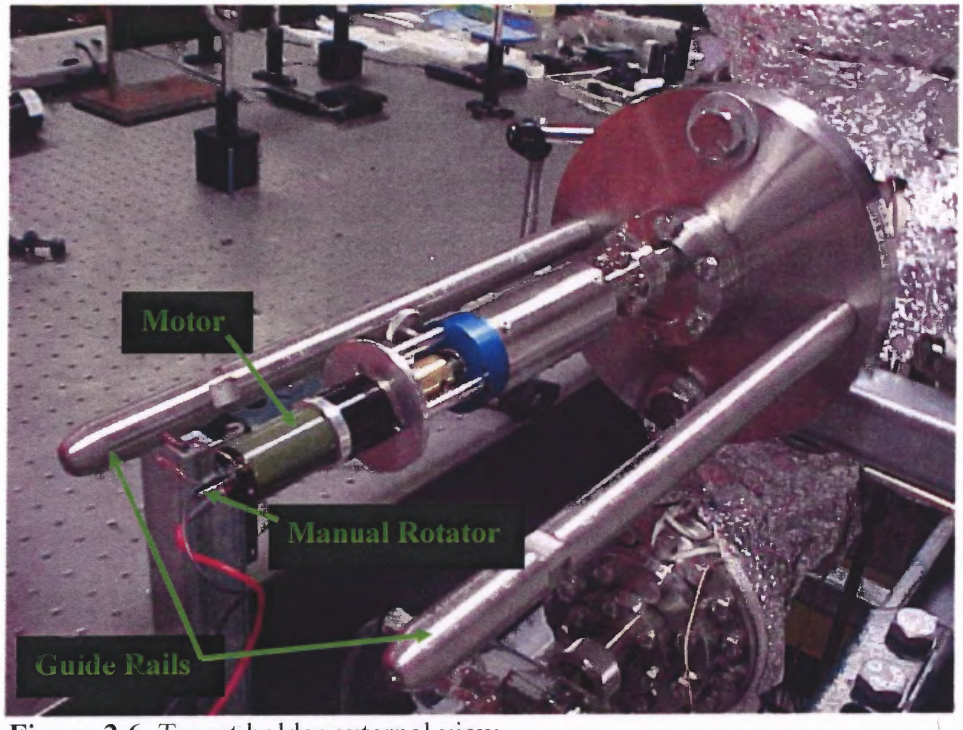

Figure 2.6 Target holder external view.

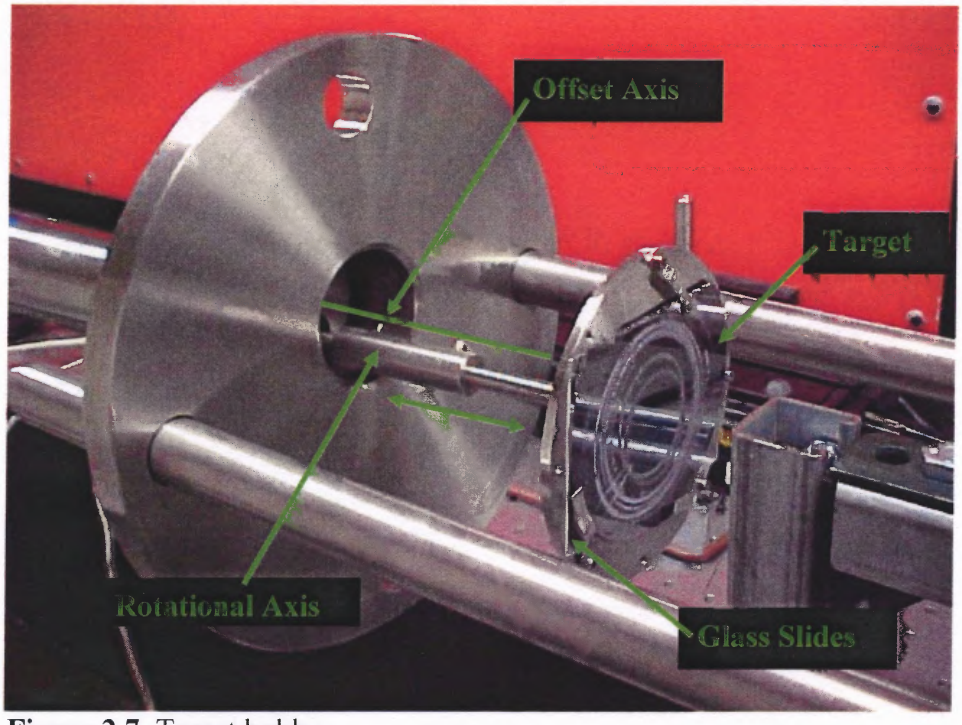

Figure 2.7 Target holder.

The substrate holder seen in Figure 2.8 can also move towards or away from the target, although this can be done under vacuum. The substrate platter can hold up to 6 samples and the substrate shield prevents deposition from occurring on the samples not behind the deposition aperture. With the chamber open to the atmosphere, the substrate shield can be easily reconfigured to accommodate various sizes of deposition area. The shield guide rails prevent the shield from moving while the platter is moved towards or away from the target. This adjustment of target-substrate separation is accomplished using the target-substrate separation knob shown in Figure 2.9. The samples can be rotated into place behind the deposition aperture via the substrate platter rotation knob seen in Figure 2.9. This can also be done under vacuum.

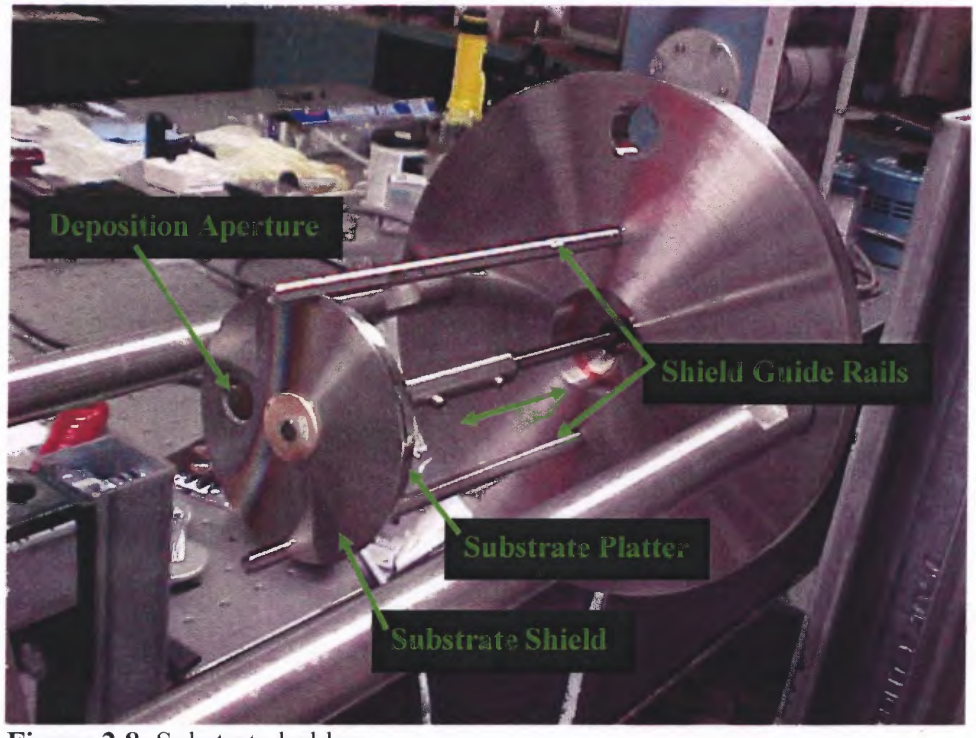

Figure 2.8 Substrate holder.

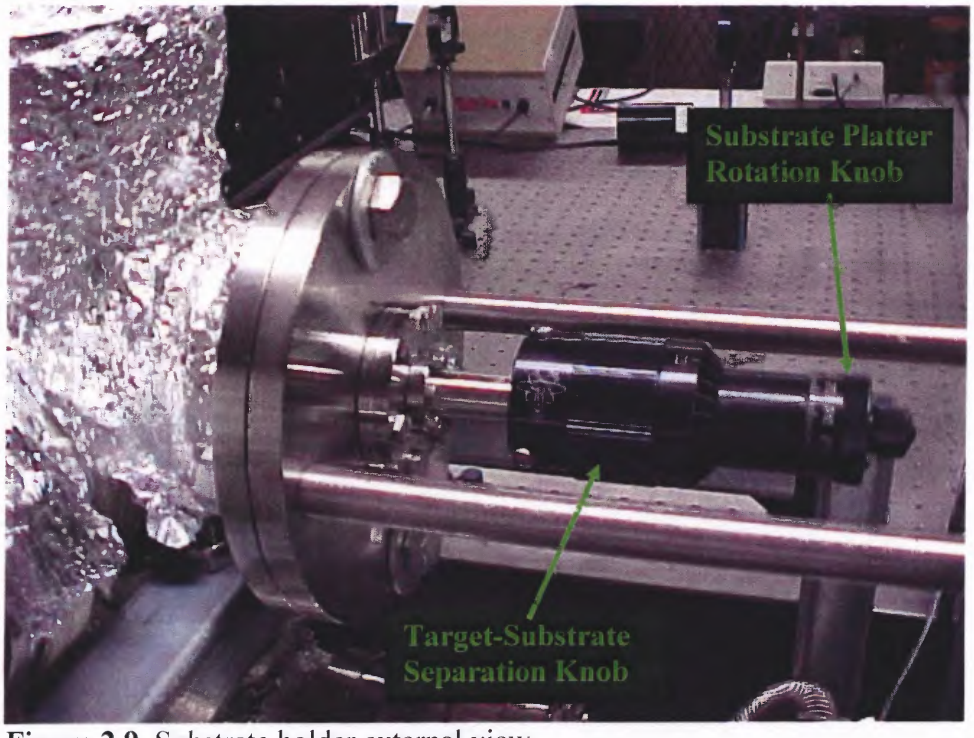

Figure 2.9 Substrate holder external view.

The optical part of the laser ablation system consists of the laser and beam focusing components shown in Figure 2.10. The beam emerges from the laser in a rectangular shape. Two cylindrical lenses and a collimating lens transform the rectangular beam laser into a Gaussian beam, which is preferred for focusing. The collimated beam is reflected towards the chamber where it is focused with a lens through the window onto the target. Initially, the beam was focused with a lens with a focal length of 15 cm. Due to the dimensions of the chamber, it was rather difficult to aim the focal point. A 20 cm focal length lens was obtained and found to be more suitable for the system.

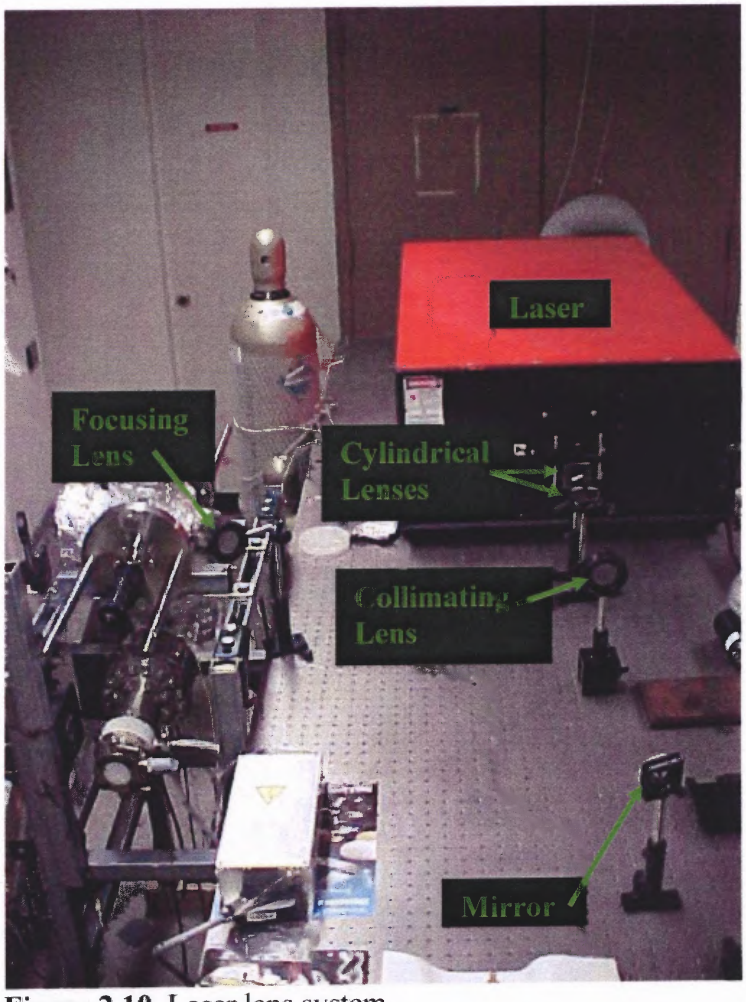

Figure 2.10 Laser lens system.

CHAPTER 3

TARGET HEATING

One of the main parameters studied for this thesis is the effect of heating the target. Due to the geometry of the chamber, it is not possible to heat the target from within the chamber. Heating the entire chamber is undesirable as it raises the pressure. The only other option at this time is optical heating. The geometry of the laboratory prevents the introduction of another laser for heating. Heat sources that were available were an arc lamp, and a halogen lamp. To make the optical heating more effective, the target was thermally insulated from the target holder by glass slides shown in Figure 2.7.

The arc lamp is an Oriel Corporation model 6140-1 mercury arc lamp operating at 150 Watts shown in Figure 3.1. The beam from the lamp was collimated with the built-in lens, then focused with an external 30 cm focal length lens.

Figure 3.1 Oriel mercury arc lamp with a focusing lens.

A higher power heat source used in the experiments was a 600 W halogen bulb. The mounting system, shown in Figures 3.2 to 3.4, had to dissipate the heat produced by the bulb and had to be able to expand with the bulb to prevent the bulb from breaking. The bulb holder was made of aluminum and the bulb housing (shown in Figures 3.3 and 3.4) was the same enclosure as that of an arc lamp with a built-in air fan.

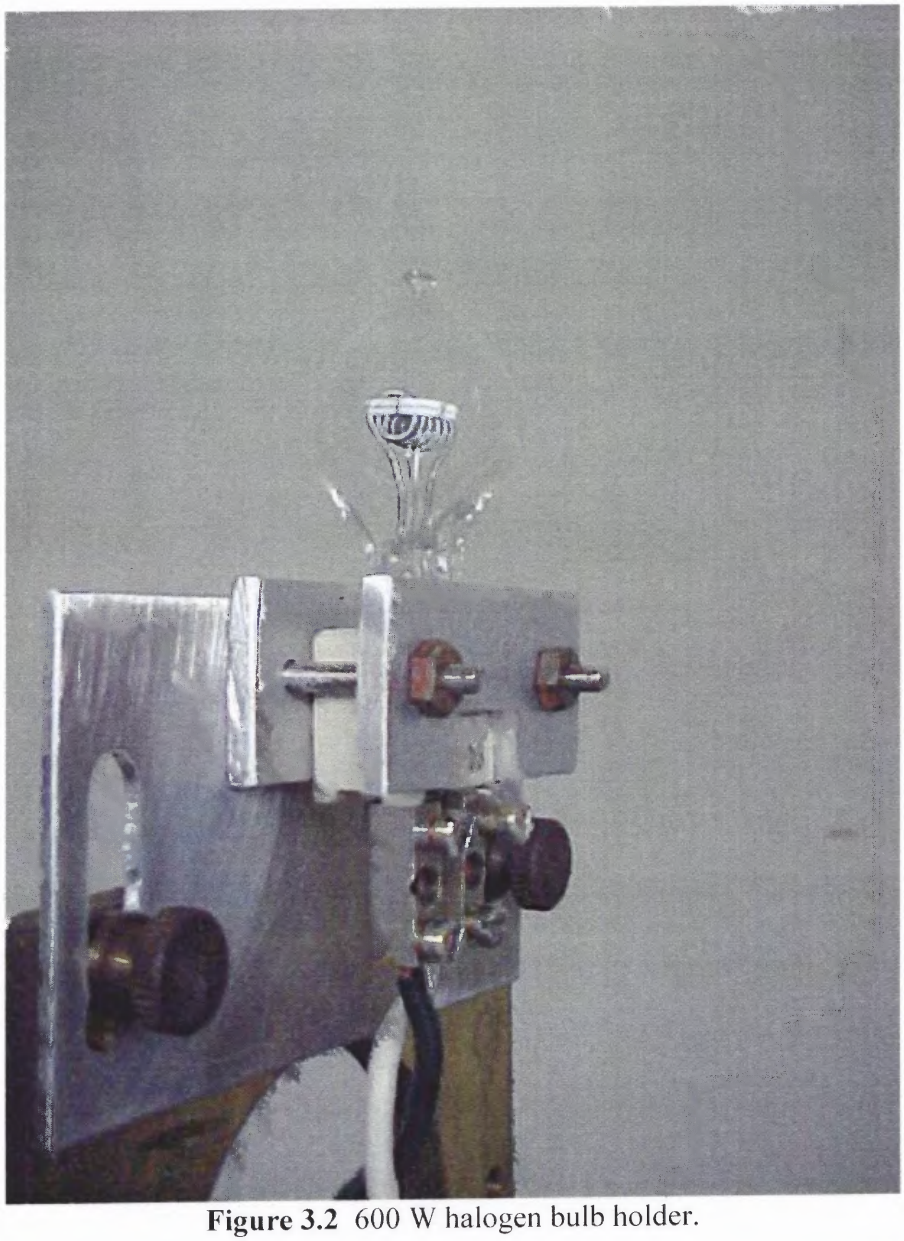

Figure 3.2 600 W halogen bulb holder.

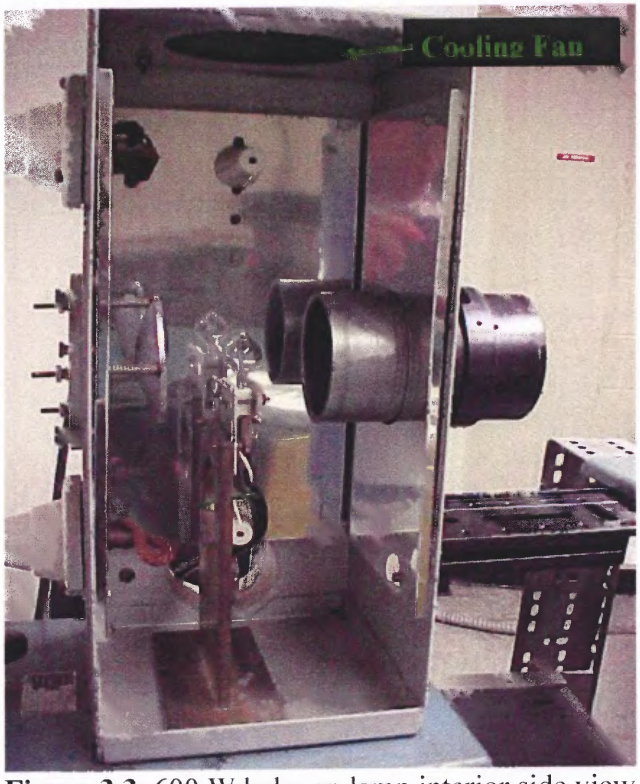

Figure 3.3 600 W halogen lamp interior side view.

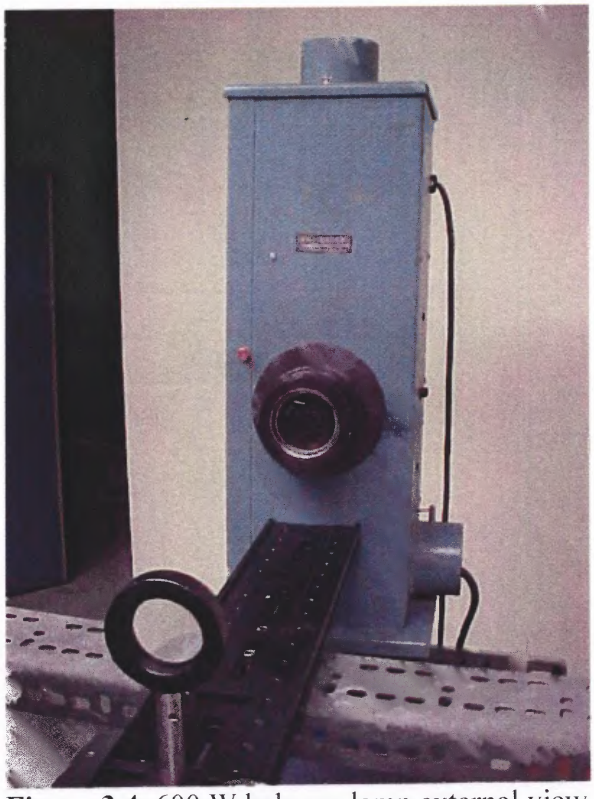

Figure 3.4 600 W halogen lamp external view.

An attempt was made to assess the effectiveness of heating with the two sources by placing a thermocouple at the focal point of the focusing lens of each source in air. The temperature the Oriel mercury arc lamp can achieve is ~70°C. The 600 W halogen bulb can achieve 200°C at the focal point of the built-in optics of the case. This focal length (~10 cm) is too short for the focal point to coincide with that of the laser beam, causing the entire target to be heated. Although very localized heating is desired for PLA, some experiments were performed with the entire target heated in this manner. Disassembly and rearrangement of the built-in optics of the case of the 600 W halogen bulb with the addition of the 30 cm focal length focusing lens yields ~50°C. Experiments were also performed with this configuration.

These temperature measurements were judged to be very inaccurate, and can be used for comparative purposes only. Manual positioning of the thermocouple at the focal point was very difficult, as even a millimeter change in position in any direction changed the temperature reading. The effectiveness of heating in vacuum cannot be ascertained from these temperature measurements since they were performed in air. Furthermore, the temperature at the tip of the thermocouple would differ from that of the target since they are made from different materials.

CHAPTER 4

RESULTS AND DISCUSSION

The following parameters can be controlled in the PLA system: deposition time, laser pulse energy, laser pulse frequency, number of pulses, target-substrate distance, target rotation, target material, substrate material, deposition area, and target heating. The experimental parameters explored in this thesis, analysis methods, and the results are presented here.

4.1 Experimental Parameters

The target material used is the silicon wafer described in Chapter 2. Its crystal orientation is not important for this research. As noted in Chapter 2, silicon with low doping was used in this work and the effects of different amounts and the kind of dopant are left for future studies. The Si target was cleaned by dipping in a HF solution, rinsing with deionized water and cleaning ultrasonically with methanol. PLA was always performed on the polished side of the wafer.

Previous studies have shown that substrate material has no effect on the structure of the deposited film [8, 9], therefore it was decided to keep the substrate the same and focus on the effect of other parameters. Glass was primarily used as the substrate for its relative flatness and low cost. Other materials such as fused silica and aluminum-coated glass were sometimes used for film characterization purposes. Glass and fused silica substrates were cleaned ultrasonically for 10 minutes with methanol or acetone.

To determine the effect of each parameter, number of pulses, deposition time, target-substrate separation, target heating, pulse frequency and target rotation were all varied individually with various sets of the other parameters. For many series of

experiments, deposition time was set constant at 10 minutes, since this was the standard for previous studies [9, 11]. Laser voltage controls the pulse energy and was varied to determine its effect. The chamber pressure was in the 2.2×10^{-7} to 5.0×10^{-7} Torr range except where noted, and was not varied.

4.2 Sample Analysis

Samples were analyzed using four different techniques. Digitally imaged optical microscopy, Raman spectroscopy, Scanning Electron Microscopy (SEM), and white light transmission were all used in this study.

4.2.1 Digitally Imaged Optical Microscopy

A reflected light microscope equipped with the KODAK© Microscopy Documentation System 290 was used to obtain digital images of the deposited films. A sample image of a deposited film is shown in Figure 4.1. The dimensions of the photographed area are 96.77 μm by 144.52 μm. The droplets are the light, roughly circular areas on the dark background. The larger droplets have a crater shape with an elevated edge and a lower, flat center. Digitally imaged optical microscopy was used to determine the effect of various parameters on the size and number of droplets deposited on the substrate. Other analysis methods were used to characterize and confirm the structure of the droplets.

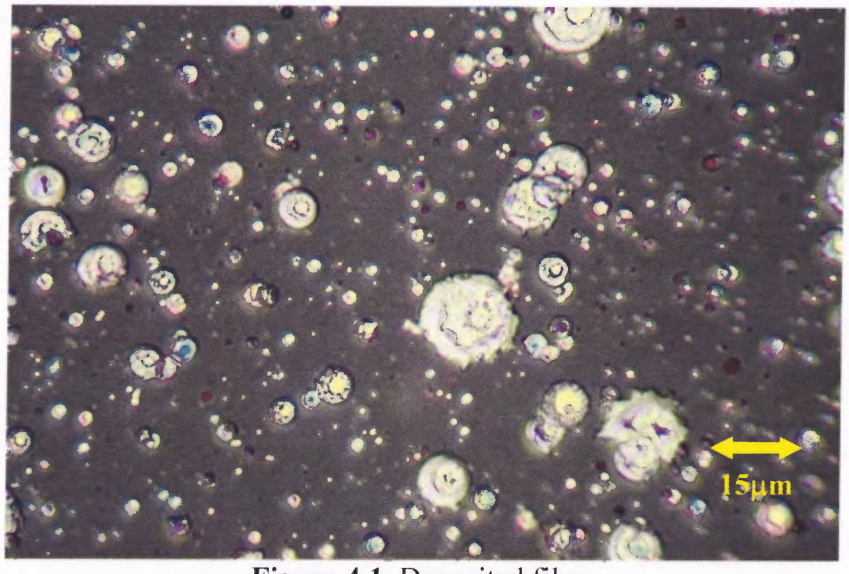

Figure 4.1 Deposited film.

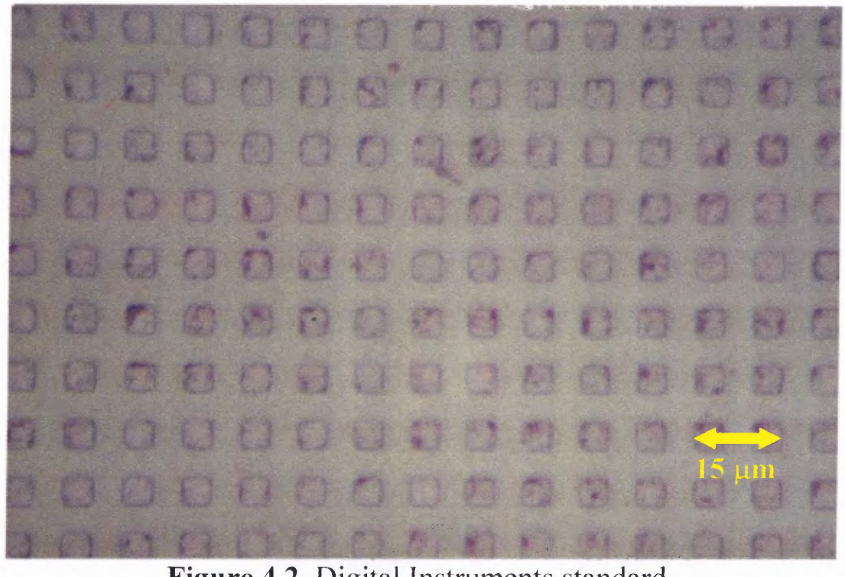

Figure 4.2 Digital Instruments standard.

Shown in Figure 4.2 is an image of the Digital Instruments standard. Adobe Photoshop 7.0 was used to develop a scale based on this standard using the fact that each square is 5 μm on a side and each square is separated from the next square by 5 μm. Droplets in the deposited films were then measured and counted manually using the Elliptical Marquee Tool in Adobe Photoshop 7.0. A sample table of droplet data is shown in Table 4.1. Droplets smaller than 1 μm were not counted. Droplet size is a diameter range from the

minimum listed to the next largest size i.e. for droplet size x, x μm ≤ droplet diameter < (x + 1) μm . The counted area was 13,985 μm^2.

Table 4.1 Sample Droplet Data.

Sample Name	Droplet Count																						
Droplet size (micrometers)	1	2	3	4	5	6	7	8	9	10	11	12	13	14	15	16	17	18	19	20	21	22	23
11-07-02 Sample 1	267	78	48	24	24	16	8	7	5	3	2	0	2	1	0	0	0	0	0	0	0	1	0
11-07-02 Sample 2	186	73	35	21	25	12	8	5	2	1	4	1	1	1	1	0	1	0	1	0	0	0	0
11-07-02 Sample 3	345	92	48	28	22	14	6	4	4	2	4	0	0	1	0	0	1	0	0	1	0	0	0
11-07-02 Sample 4	269	65	55	28	24	15	7	7	3	2	1	1	2	0	0	0	0	1	0	0	0	0	0
11-07-02 Sample 5	30	1	2	1	1	2	0	0	0	0	0	0	0	0	0	0	0	0	0	0	0	0	0

For all the following graphs, a "still target" denotes that the target was moved periodically by hand to avoid drilling through the target. A "rotating target" refers to a target rotating at a constant speed of ~120 RPM or ~4 RPM. Since no data sets had comparable conditions for studying the effect of rotational speed, speed was not noted. Wherever number of pulses is noted, the target was not moved at all so that the laser pulses would be incident on the same spot.

4.2.1.1 Effect of Laser Lens Arrangement. To determine the optimal lens arrangement with the available lenses, experiments were performed with two arrangements. The collimating lens and the focusing lens serve different purposes in the system but can be interchanged. One lens has a focal length of 15 cm while the other lens has a focal length of 10 cm. The two arrangements were the two possible combinations of the two interchangeable lenses. The graph in Figure 4.3 compares the effects of those arrangements.

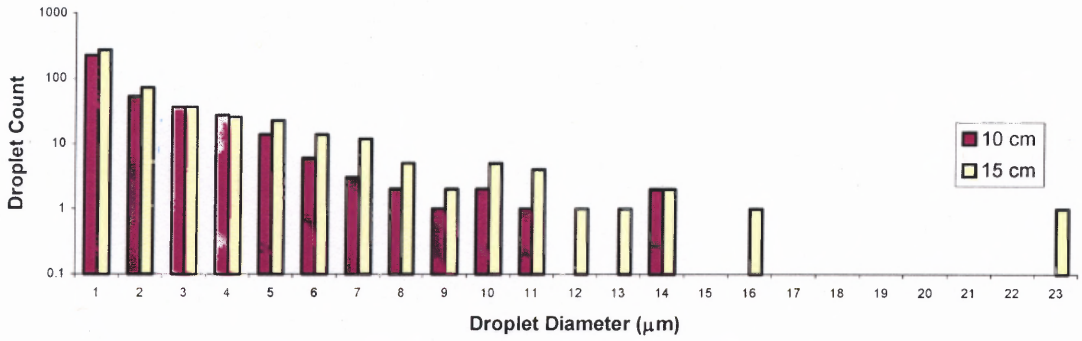

Figure 4.3 Effect of lens arrangement (focal length of focusing lens labeled). Number of droplets versus droplet diameter. 10 min deposition time. Still target. Unheated. 24 kV laser pulse power. 20 Hz laser pulse frequency.

The 15 cm focusing lens generates the maximum droplet diameter (23 μm) which is 9 μm larger than the maximum for the 10 cm focusing lens. The arrangement with the 15 cm focusing lens also creates more droplets with 15 droplets greater than or equal to 10 μm in diameter in comparison to 5 droplets for the arrangement with the 10 cm focusing lens.

4.2.1.2 Effect of Target Rotation. Experiments were performed to determine the effect of target rotation. The target was either rotated with the motor or moved slightly periodically by hand to avoid drilling through the target (labeled as "still"). The results are shown in Figure 4.4.

The pressure during deposition for the experiment represented in Figure 4.4A was the highest of all experiments by one order of magnitude (3.0×10^{-6} Torr whereas all other pressures were within 2.2×10^{-7} – 5.0×10^{-7} Torr). This was due to the lack of overnight baking of the chamber during preliminary testing of the system. The effect of the chamber pressure was not studied for this thesis and the pressure for this experiment was only noted for the record. Figure 4.4 shows that a rotating target yields smaller

maximum droplet diameter and fewer large droplets than a still target regardless of the laser pulse frequency. Figure 4.4A, B, and C were different experiments under the same conditions.

Figure 4.4A shows that a still target yields 14 droplets greater than or equal to 10 μm in diameter while a rotating target yields only 1 droplet.

Figure 4.4B shows that a still target yields 4 droplets greater than or equal to 10 μm in diameter while a rotating target yields none.

Figure 4.4C shows that a still target yields 5 droplets greater than or equal to 10 μm in diameter and a rotating target yields none.

Figure 4.4D shows that for a higher pulse frequency of 40 Hz, a still target yields 1 droplet greater than or equal to 10 μm in diameter while a rotating target yields none.

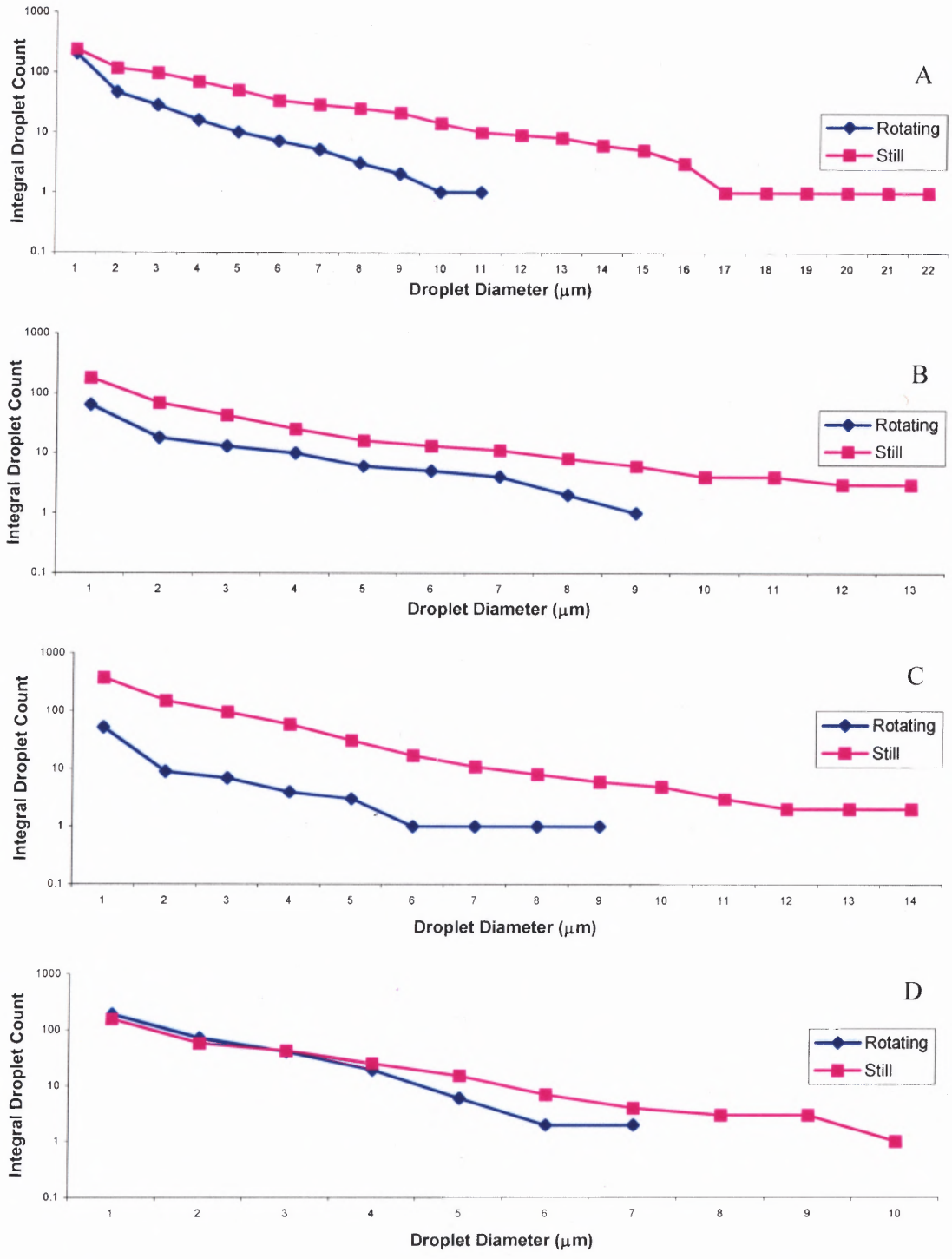

Figure 4.4 Effect of target rotation. Number of droplets greater than or equal to a given diameter versus droplet diameter. 10 min deposition time. Unheated. 24 kV laser pulse power. A, B and C: 20 Hz laser pulse frequency. D: 40 Hz laser pulse frequency.

4.2.1.3 Effect of Laser Pulse Power. The effect of laser pulse power was studied under various sets of conditions. As noted in Section 4.1 laser pulse power is controlled by laser voltage. The results of experiments with a voltage of 24 kV (the maximum voltage for the laser) were compared with those of a lower voltage of 20 kV and 17 kV in Figure 4.5.

Figure 4.5A shows that higher laser pulse power yields a larger maximum droplet diameter (36 μm) than lower laser pulse power (26 μm).

Figure 4.5B shows that higher laser pulse power yields a larger maximum droplet diameter (38 μm) than lower laser pulse power (27 μm).

Figure 4.5C shows that higher laser pulse power yields a larger maximum droplet diameter (31 μm) than lower laser pulse power (24 μm).

Figure 4.5D shows that higher laser pulse power yields a larger maximum droplet diameter (49 μm) than lower laser pulse power (30 μm).

Figure 4.5 shows that higher power yields the largest droplet diameter. Comparison of graphs A with D and B with D shows that this trend exists independently of target heating.

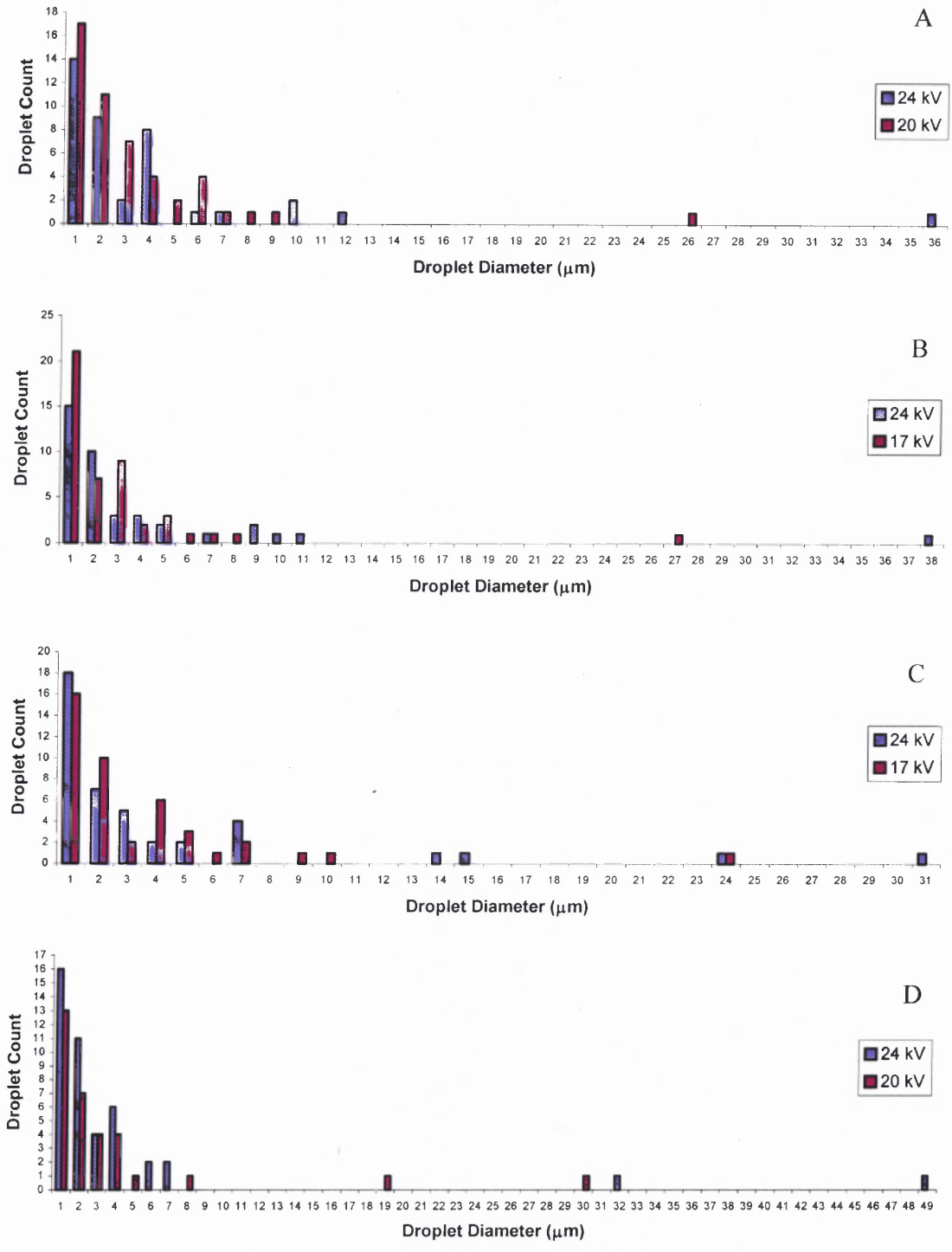

Figure 4.5 Effect of laser pulse power. Number of droplets versus droplet diameter. A: 1000 pulses. Unheated. 35.0 mm target-substrate separation. B: 1000 pulses. Unheated. 35.0 mm target-substrate separation. C: 1000 pulses. Unheated. 32.6 mm target-substrate separation. D: 1000 pulses. Heated. 35.0 mm target-substrate separation.

4.2.1.4 Effect of Laser Pulse Frequency. The effect of laser pulse frequency was studied under various sets of parameters.

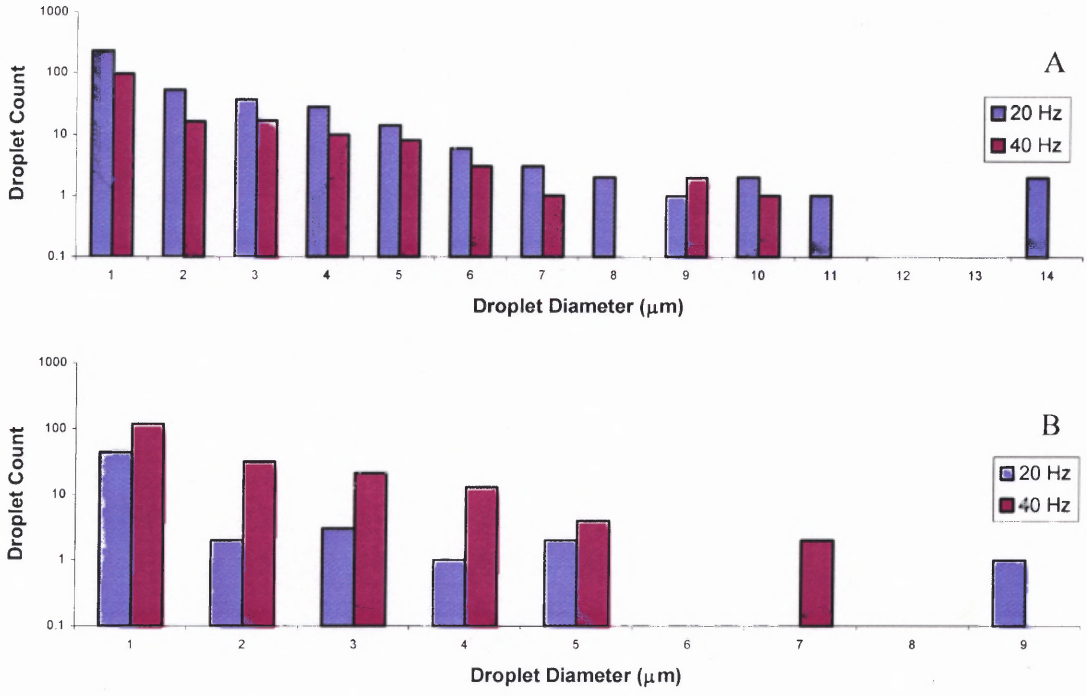

Figure 4.6 Effect of laser pulse frequency. Number of droplets versus droplet diameter. 10 min deposition time. Unheated. 24 kV laser pulse power. A: Still target. B: Rotating target.

Figure 4.6A shows that lower frequency yields the droplets of maximum diameter. Figure 4.6B also shows that lower frequency yields the droplets of maximum diameter. Although Figure 4.6 shows that lower pulse frequency yields the largest droplets regardless of target rotation, there are inconsistencies that belie this hypothesis. One would expect the higher frequency to yield a higher total number of droplets than a lower frequency, but this is not true for graph A. Graph B and Figure 4.7 exhibit the trend of increased droplet total with increasing laser pulse frequency.

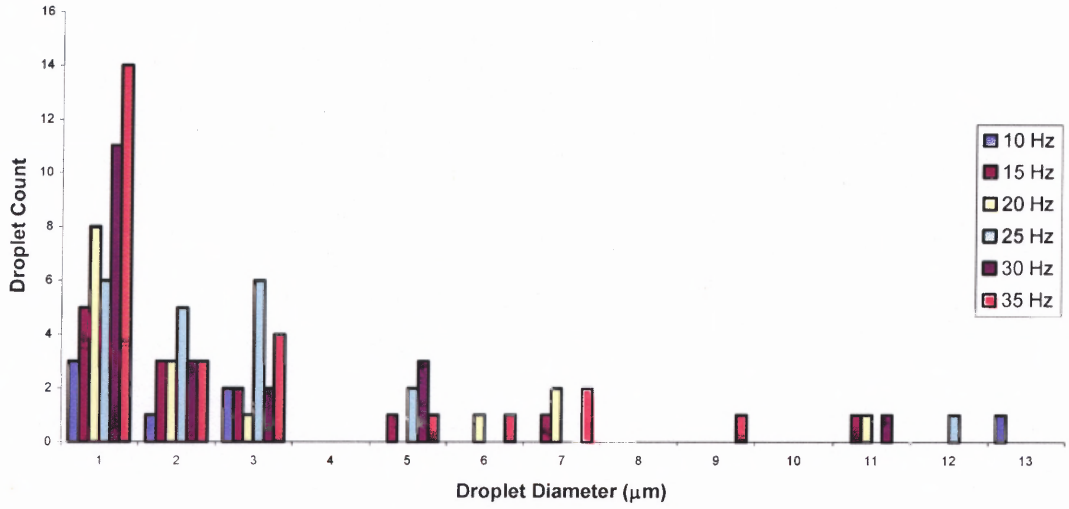

Figure 4.7 Effect of laser pulse frequency. Number of droplets versus droplet diameter. 10 min deposition time. Rotating target. Unheated. 24 kV laser pulse power.

Figure 4.7 shows that the number of droplets greater than or equal to 10 μm in diameter is the same for all frequencies. Only the total number and number of smaller droplets increases with frequency.

4.2.1.5 Effect of Deposition Time. The effect of deposition time was studied for various sets of parameters. For Figure 4.8, deposition time was varied from 30 seconds to 8 minutes.

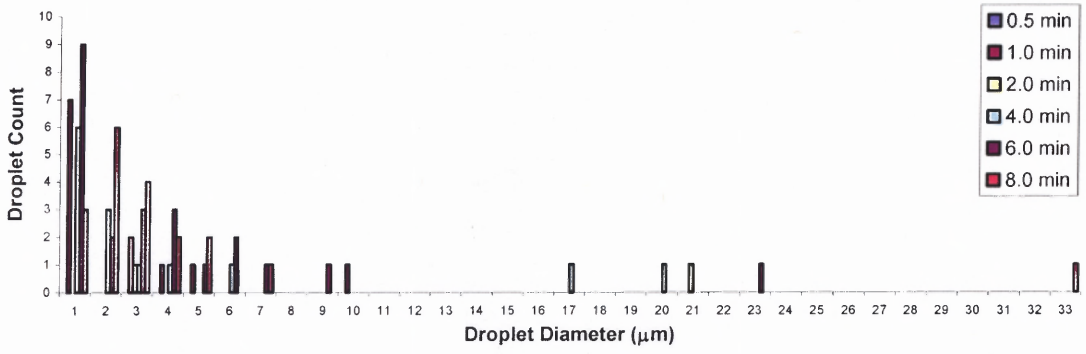

Figure 4.8 Effect of deposition time. Number of droplets versus droplet diameter. Rotating target. Unheated. 24 kV laser pulse power. 20 Hz laser pulse frequency.

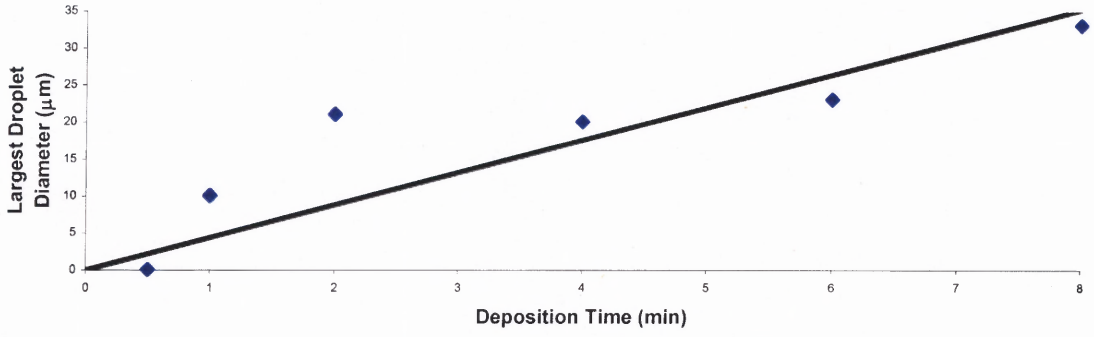

Figure 4.9 Largest droplet diameter versus deposition time for series in Figure 4.8.

Figures 4.8 and 4.9 show that as deposition time increases, droplet maximum diameter increases. The largest droplets appear with relatively low probability and their appearance is more likely at longer deposition times.

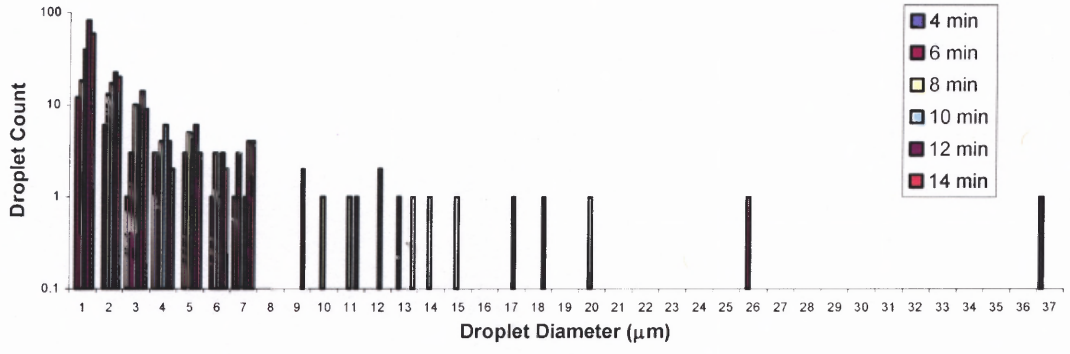

Figure 4.10 Effect of deposition time. Number of droplets versus droplet diameter. Rotating target. Heated. 24 kV laser pulse power. 20 Hz laser pulse frequency. 35.0 mm target-substrate separation.

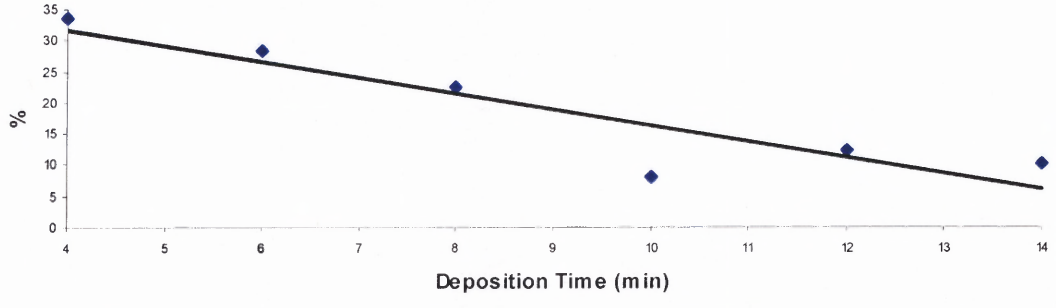

Figure 4.11 Linear fit of percentage of number of droplets greater or equal to 5 μm in diameter of total droplets versus deposition time for series in Figure 4.10.

Figure 4.11 shows that as deposition time increases, the percentage of droplets greater than or equal to 5 μm in diameter of total droplets decreases. This is caused by the increase in the number of small droplets with increasing time. The total number of droplets increases faster than the number of droplets greater than or equal to 5 μm in diameter, causing the percentage of droplets greater than or equal to 5 μm in diameter to decrease.

The discernable trend in Figure 4.11 may also be due to erosion of the target. All samples represented in Figure 4.11 were deposited without changing the position of the laser beam, i.e. from the same track on the target. The progressive erosion of the target on the laser beam track results in increasing amounts of smaller droplets. Although a definite conclusion cannot be made, it seems likely that increased deposition time results in larger droplets until a point at which target erosion causes droplet size to decrease.

4.2.1.6 Effect of Number of Pulses. This series of studies focused on the effect of number of incident pulses on a single spot on the target. Target rotation was removed to study this effect. Laser pulse frequency and deposition time were varied according to the number of required pulses, but were not taken into consideration in the results. For the most part, laser pulse frequency was maintained at 10 Hz, except when 10 pulses were required in which case 1 Hz was used.

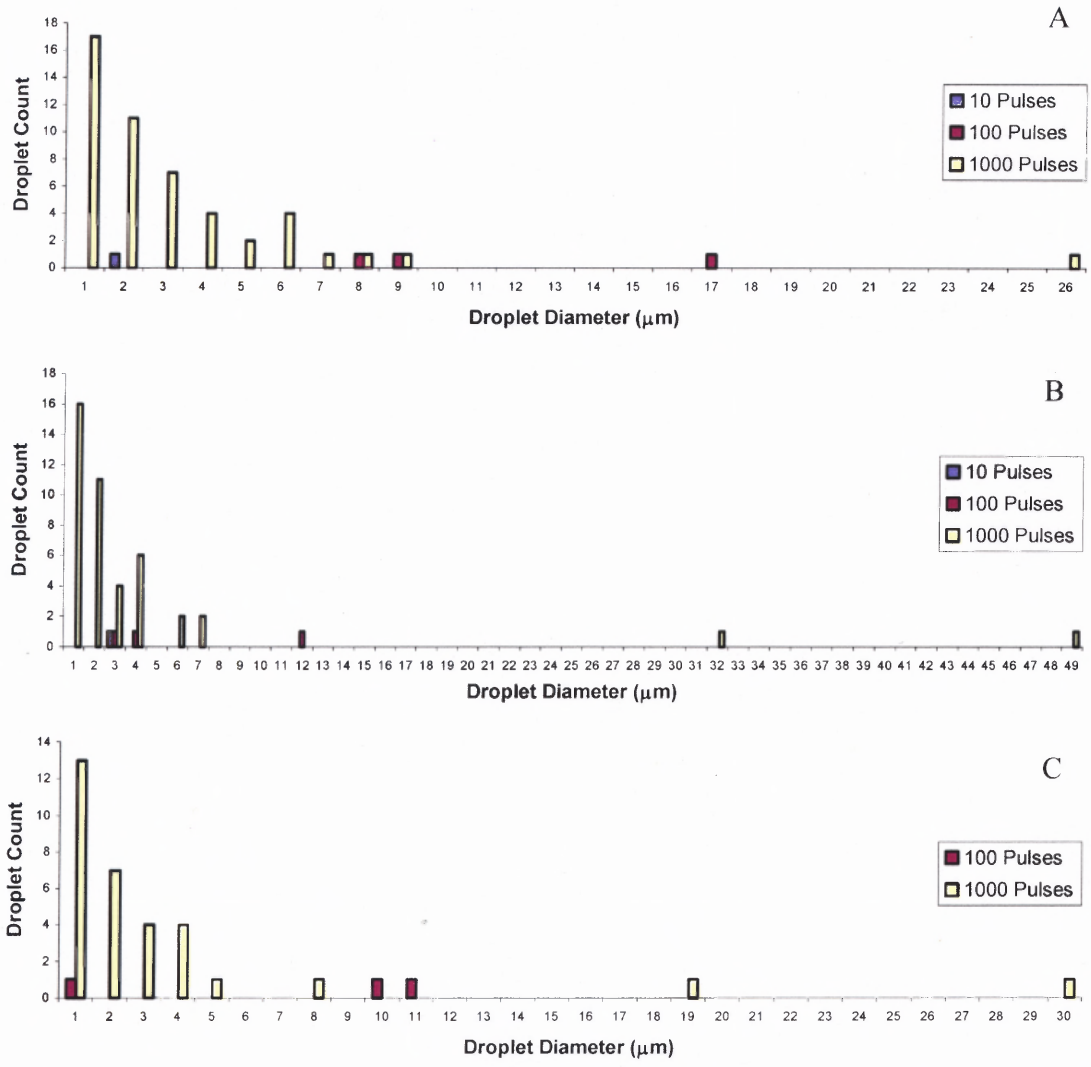

Figure 4.12 Effect of number of pulses. Number of droplets versus droplet diameter. 35.0 mm target-substrate separation. A: Unheated. 20 kV laser pulse power. B: Heated. 24 kV laser pulse power. C: Heated. 20 kV laser pulse power.

Figures 4.12A with 4.12B and Figures 4.12C with 4.12D show that largest droplet diameter increases with number of pulses regardless of laser pulse power.

Figures 4.12A with 4.12C and Figures 4.12B with 4.12D show that largest droplet diameter increases with number of pulses regardless of target heating.

Figure 4.12 shows that up to 1000 pulses, the largest droplet diameter increases with number of pulses. There may a maximum number of pulses beyond which droplet diameter decreases as the target becomes eroded.

4.2.1.7 Effect of Target-Substrate Separation. Target-substrate distance was varied to determine its effect on droplet size. Figure 4.13 shows the results of target-substrate separation varying from 23.6 mm to 30.8 mm.

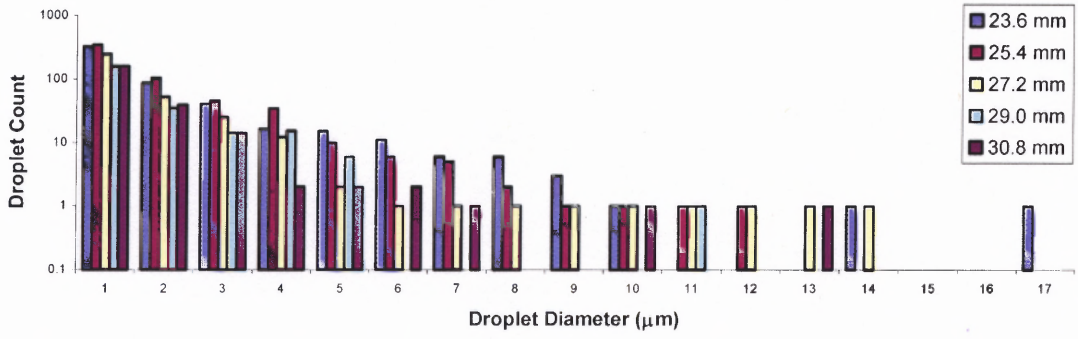

Figure 4.13 Effect of target-substrate separation. Number of droplets versus droplet diameter. 10 min deposition time. Still target. Unheated. 24 kV laser pulse power. 20 Hz laser pulse frequency.

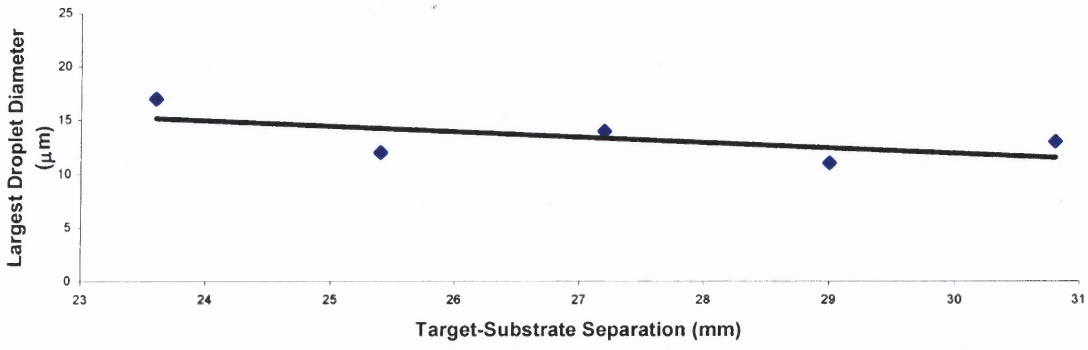

Figure 4.14 Linear fit for largest droplet diameter versus target-substrate separation for series in Figure 4.13.

Figure 4.13 shows that the shortest target-substrate separation yields the droplets of largest diameter. This effect can be seen in Figure 4.14 which shows that the largest

droplet diameter increases as target-substrate separation decreases, but this dependence is not very strong based on the low slope of the linear fit.

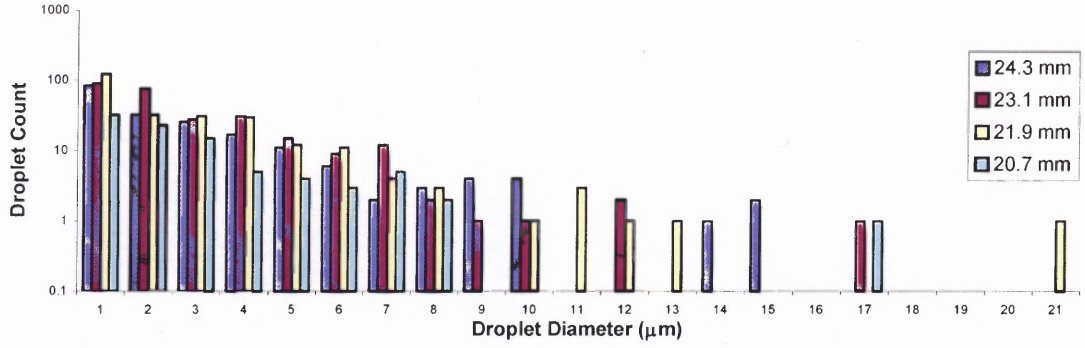

Figure 4.15 Effect of target-substrate separation. Number of droplets versus droplet diameter. 10 min deposition time. Still target. Heated. 24 kV laser pulse power. 20 Hz laser pulse frequency.

Figure 4.15 shows that as target-substrate separation decreases from 24.3 mm to 21.9 mm, largest droplet diameter increases. However, at the shortest target-substrate separation (20.7 mm), the largest droplet diameter decreases.

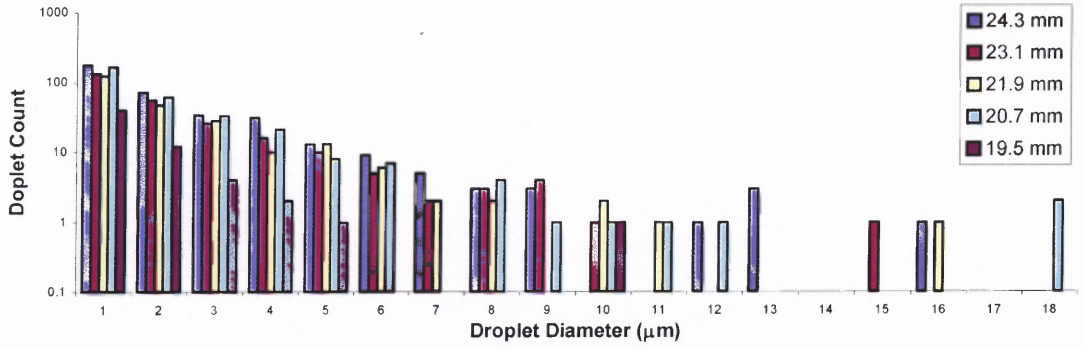

Figure 4.16 Effect of target-substrate separation. Number of droplets versus droplet diameter. 10 min deposition time. Still target. Unheated. 24 kV laser pulse power. 20 Hz laser pulse frequency.

Figures 4.16 shows that as target-substrate separation decreases from 24.3 mm to 21.9 mm, largest droplet diameter increases. However, as target-substrate separation

decreases from 21.9 mm to 19.5 mm, largest droplet diameter decreases. This is in agreement with the results from Figure 4.15.

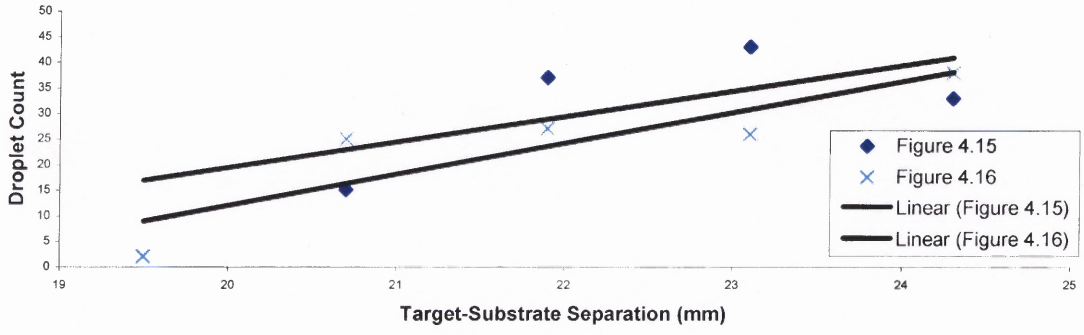

Figure 4.17 Number of droplets greater than or equal to 5 μm in diameter versus target-substrate separation for series in Figures 4.15 and 4.16.

An interesting result from Figures 4.15 and 4.16 is shown in Figure 4.17. The number of droplets greater than or equal to 5 μm in diameter appears to increase with increasing target-substrate separation. This may indicate that larger droplets form from longer time of flight, though this is only speculation. The data was inconsistent, making it impossible to draw any conclusions on the effect of target-substrate separation.

4.2.1.8 Effect of Heating. The effect of heating was studied with different sets of parameters and different heat sources. Figure 4.18 shows the effect of heating for various target-substrate separations.

Figure 4.18 shows that heating does not have a noticeable effect. It does not consistently produce the largest droplets, nor does it consistently affect the total number of droplets. The number of droplets greater than or equal to 5 μm in diameter is also independent of heating.

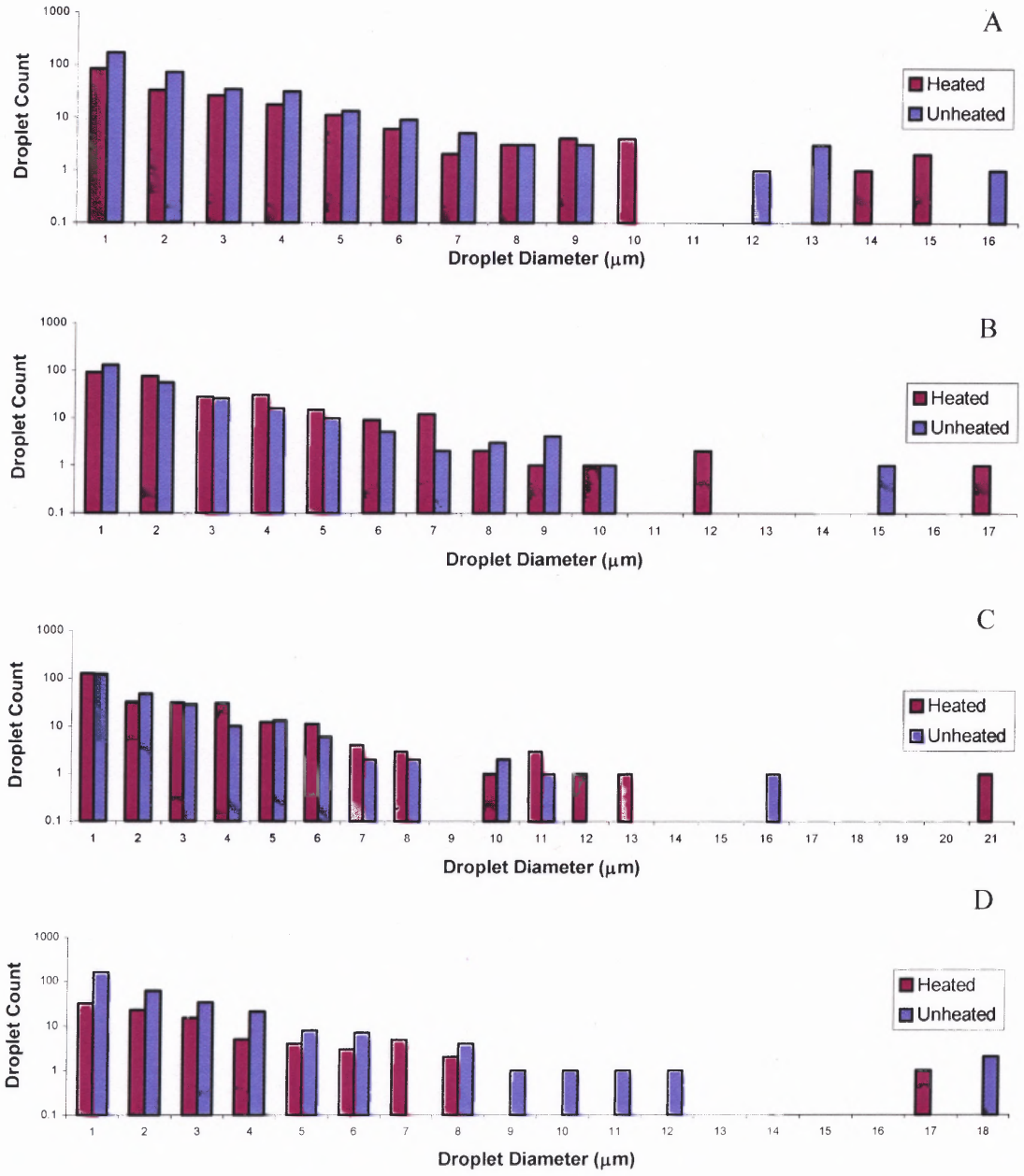

Figure 4.18 Effect of target heating. Number of droplets versus droplet diameter. 10 min deposition time. Still target. 24 kV laser pulse power. 20 Hz laser pulse frequency. A: 24.3 mm target-substrate separation. B: 23.1 mm target-substrate separation. C: 21.9 mm target-substrate separation. D: 20.7 mm target-substrate separation.

The effect of heating for various deposition times is studied in Figure 4.19.

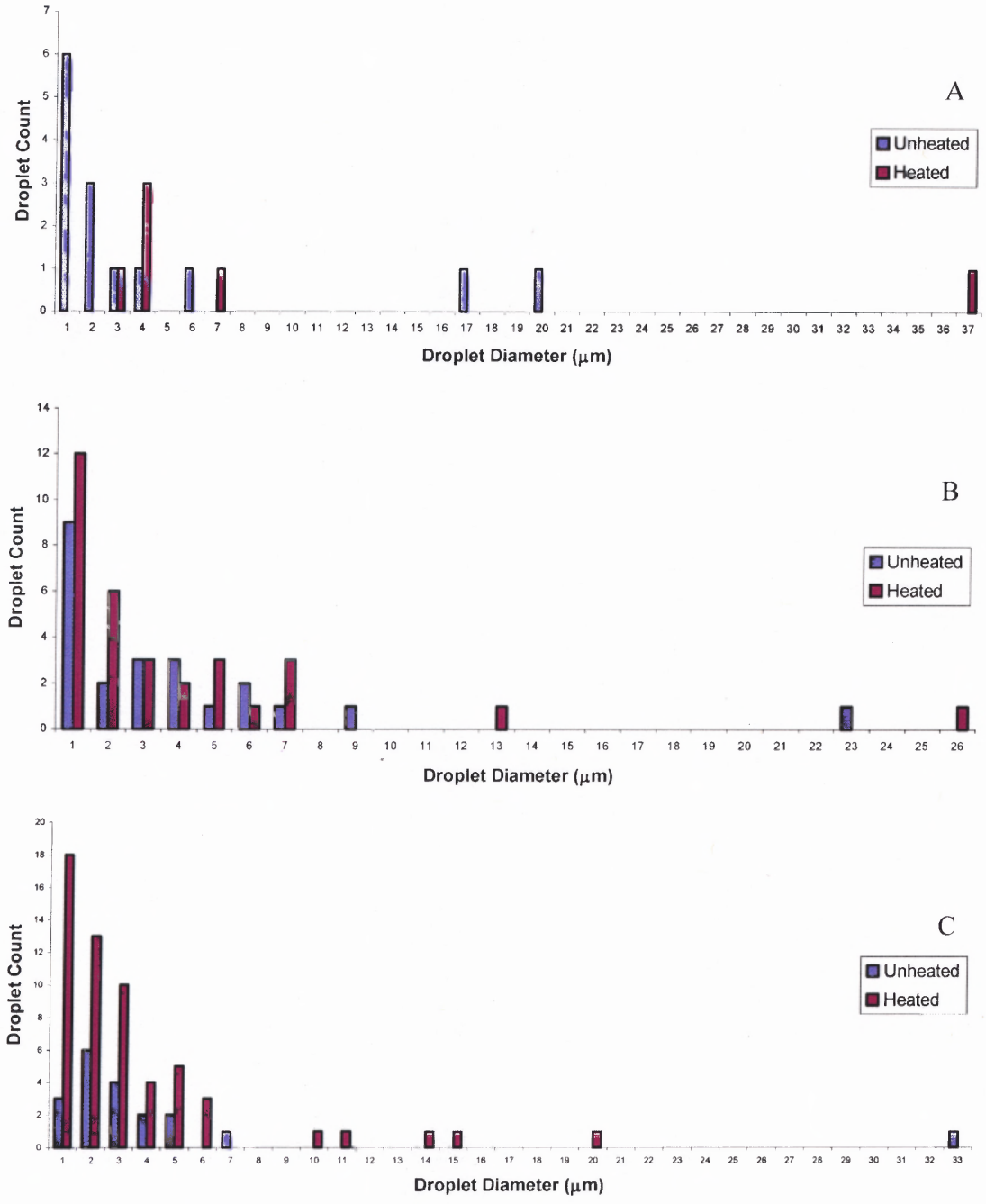

Figure 4.19 Effect of heating. Number of droplets versus droplet diameter. Rotating target. 24 kV laser pulse power. 20 Hz laser pulse frequency. A: 4 min deposition time. B: 6 min deposition time. C: 8 min deposition time.

The results of Figure 4.19 are also inconclusive. Heating does not consistently produce the largest droplets nor does it consistently create a larger total number of droplets.

Figure 4.20 studies the effect of heating for various laser pulse powers.

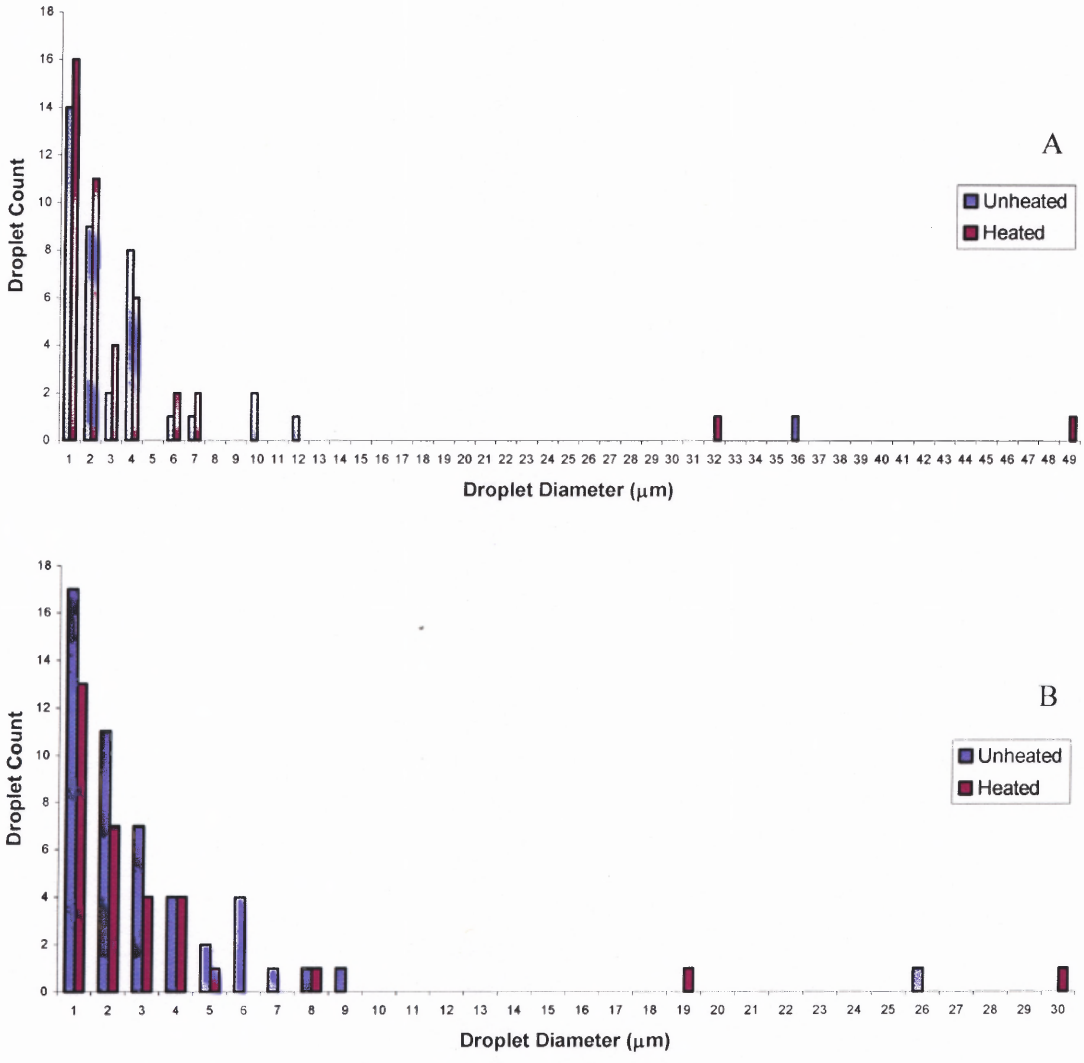

Figure 4.20 Effect of heating. Number of droplets versus droplet diameter. 35.0 mm target-substrate separation. 10 Hz laser pulse frequency. 1000 pulses. A: 24 kV laser pulse power. B: 20 kV laser pulse power.

Figure 4.20 shows that for 1000 pulses, heating produces the largest droplet diameter regardless of laser pulse power, but heating does not consistently create a larger or smaller number of total droplets.

4.2.2 Raman Spectroscopy

Raman spectroscopy was performed on all the deposited films to verify their structure as hexagonal. One expects three lines in the Raman spectra for hexagonal-wurtzite Si, but due to the closeness of the peaks, the result is a single broadened line [8, 12]. Cubic-diamond Si exhibits a 520 cm^{-1} Raman shift while typically hexagonal Si exhibits a 516cm^{-1} shift [13]. A Si wafer was used as the standard to determine the location of the cubic-diamond Si peak and a 4 cm^{-1} shift from that peak signifies the presence of hexagonal Si. The following figure is the Raman spectra of the Si standard for a particular day's measurement.

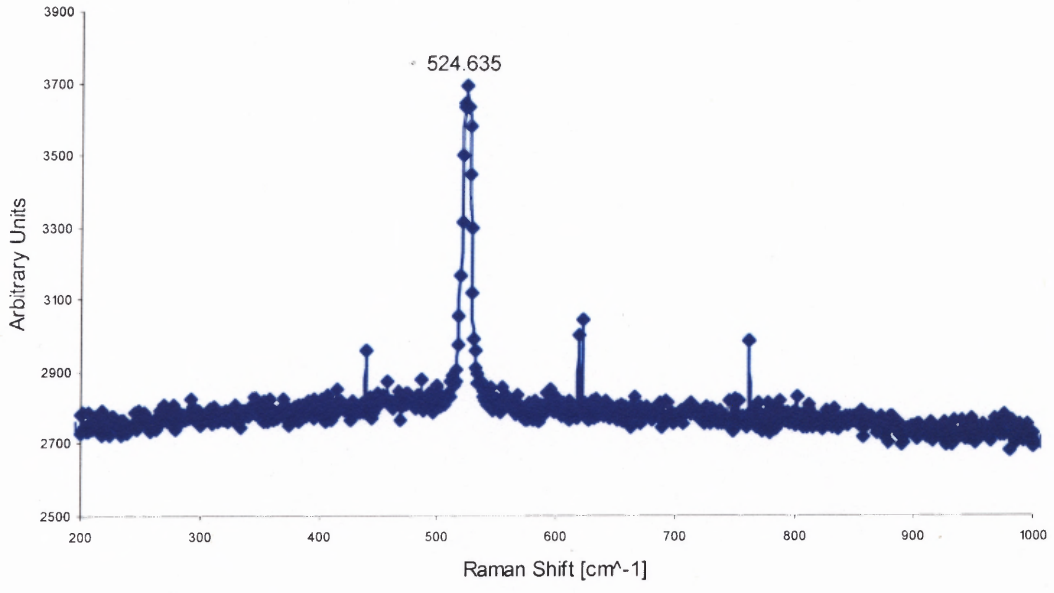

Figure 4.21 Cubic-diamond Si standard Raman spectra.

The cubic-diamond Si peak occurs at 524 cm^{-1} for the Raman system used for this thesis, therefore the hexagonal peak is expected to occur at around 520 cm^{-1}. The following figure is the Raman spectra from the same day for one of the laser ablation deposited films.

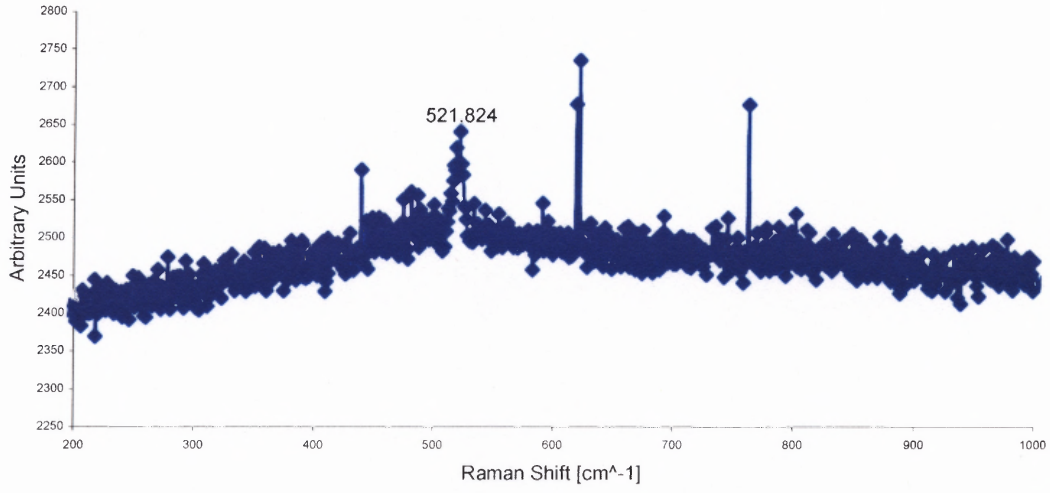

Figure 4.22 Deposited film Raman spectra.

A peak occurs at around 521cm^{-1} and is broader and less intense than the cubic-diamond Si peak. This is what is expected for hexagonal Si.

Almost all deposited films showed the same peak with a 4 cm^{-1} difference from the standard. In some measured spectra the hexagonal Si peak was not found. This may be explained by the fact that the incident laser beam in the Raman spectrometer was not aimed onto a droplet of hexagonal silicon.

4.2.3 Scanning Electron Microscopy

To obtain a more detailed understanding of their structure, some samples of the films were examined using Scanning Electron Microscopy (SEM). Figure 4.23 and 4.24 are sample SEM images of a deposited film.

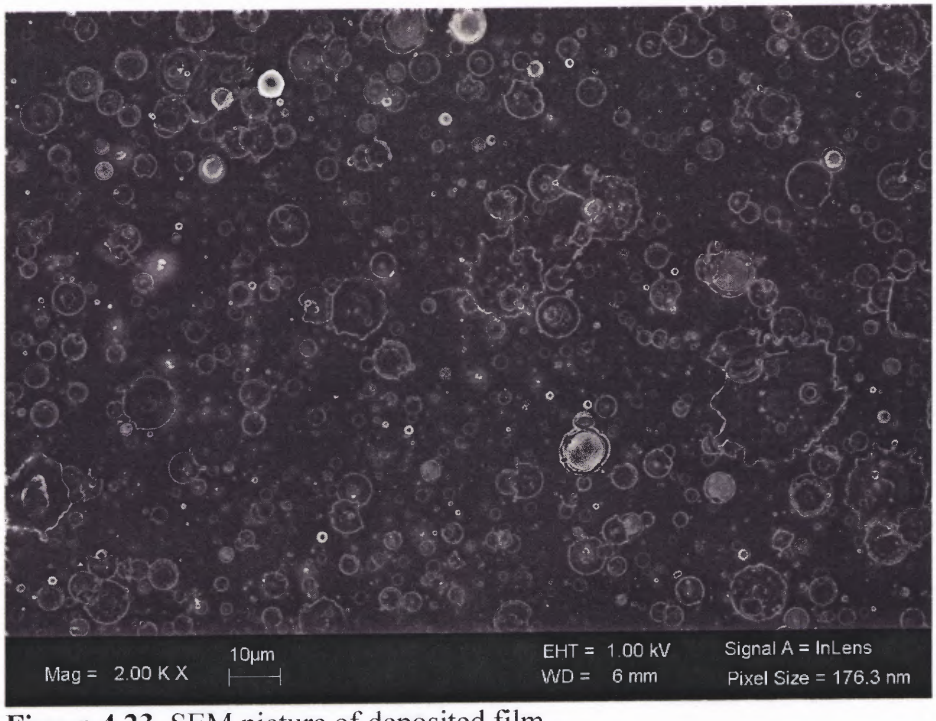

Figure 4.23 SEM picture of deposited film.

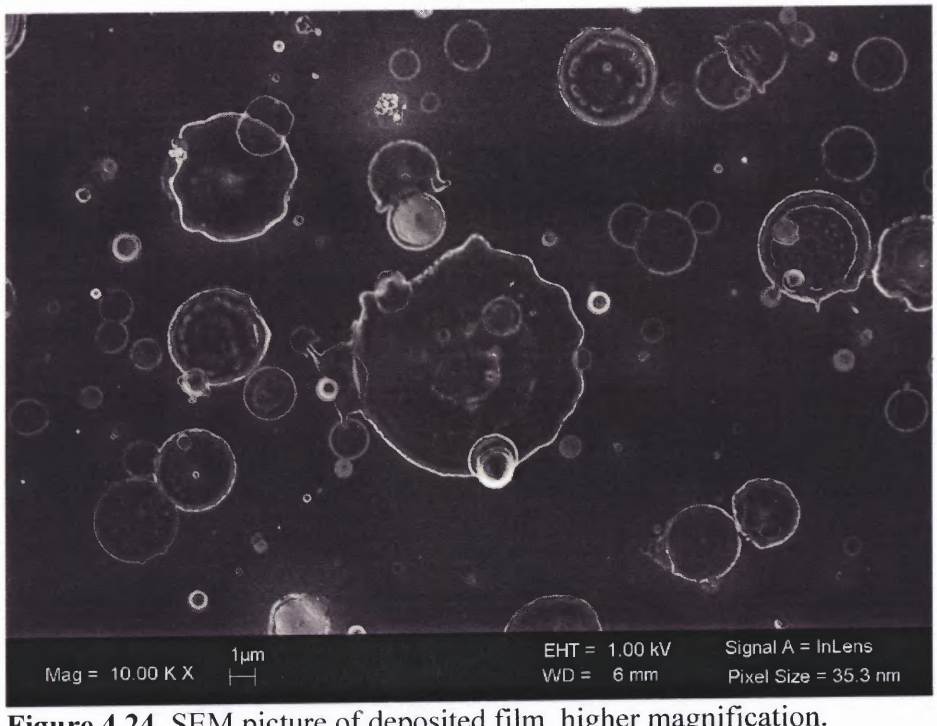

Figure 4.24 SEM picture of deposited film, higher magnification.

From these images, the three-dimensional structure of the droplets is more apparent than from optical microscopy. The larger droplets exhibit the concave crater shape while the smaller droplets appear to be more convex in their centers or sometimes even conical. SEM microscopy could have been used for determining the size distribution of the droplets, but was forgone for convenience purposes. The SEM is not readily available for use and samples would have to either be on a conductive substrate or coated with amorphous carbon to obtain an image. Coating with amorphous carbon would prevent the use of other analysis methods as well.

4.2.4 White Light Transmission

White light transmission spectra were taken for a thick sample for different incident light polarizations and angles using the following setup.

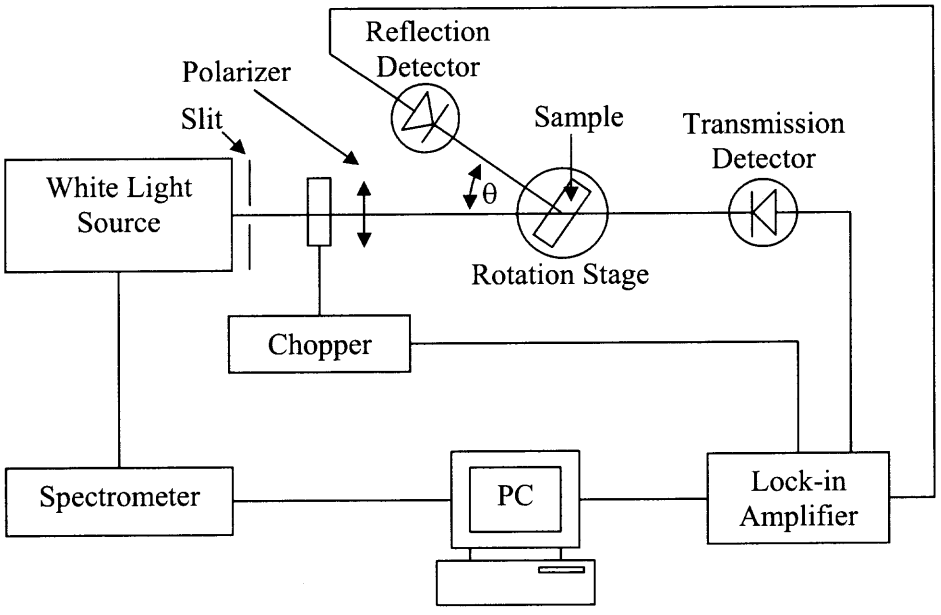

Figure 4.25 White light transmission top view diagram.

Transmission spectra were also taken for plain glass substrate as reference. Incident light was parallel or perpendicularly polarized with respect to the plane of incidence. The sample was tilted at angle θ = 0°, 10°, and 50° with respect to the incident light about an axis normal to the plane of incidence. Since the hexagonal crystals have been shown to have a preferred <111> orientation [9, 10], it is expected that the transmission spectra of one polarization should not be affected by changing the incidence angle while the transmission spectra of the other polarization will.

The grating used for the following figures was 600 lines/mm. Figure 4.26 compares the spectra for parallel polarization and perpendicular polarization for each angle for 800 to 1600 nm wavelength. Figure 4.27 compares the spectra for each angle at a particular polarization for 800 to 1600 nm wavelength. Figure 4.27 shows that the transmission spectra for perpendicularly polarized light does not change with angle, but the transmission for parallel polarized light does change for the 50° tilt. This result agrees with what was expected.

In Figure 4.28 the absorption was calculated as $A = -\ln T$ where A is the absorption and T is the transmission.

Figure 4.29 compares the spectra for parallel polarization and perpendicular polarization for each angle for 575 to 900 nm wavelength. Figure 4.30 compares the spectra for each angle at a particular polarization for 575 to 900 nm wavelength. Figure 4.30 shows that the transmission spectra for perpendicularly or parallel polarized light does not change with angle. Although the 600 lines/mm grating should allow accurate readings down to 500 nm wavelength, below 575 nm the signal was too noisy.

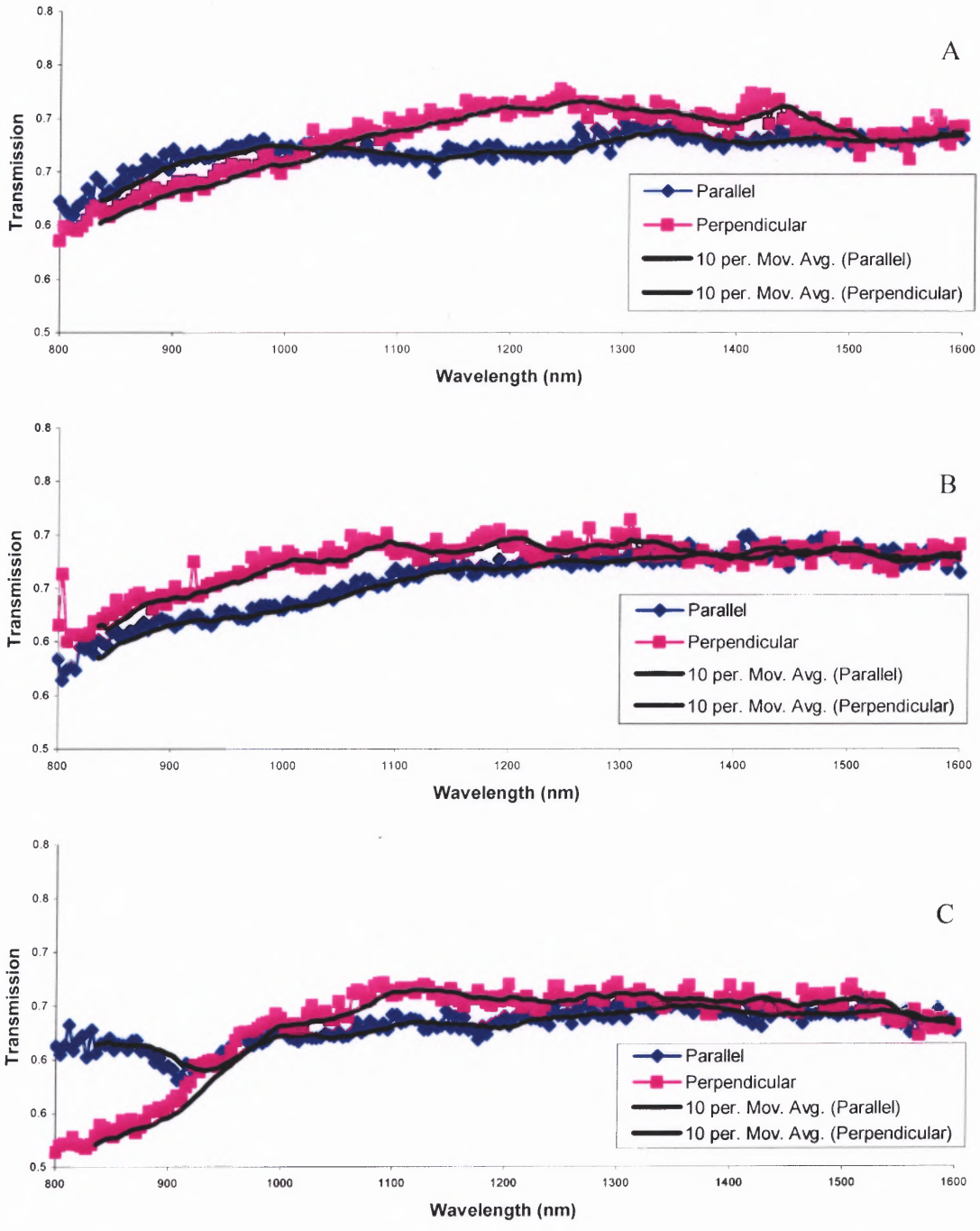

Figure 4.26 White light transmission spectra for 800 to 1600 nm wavelength. A: $\theta = 0°$. B: $\theta = 10°$. C: $\theta = 50°$

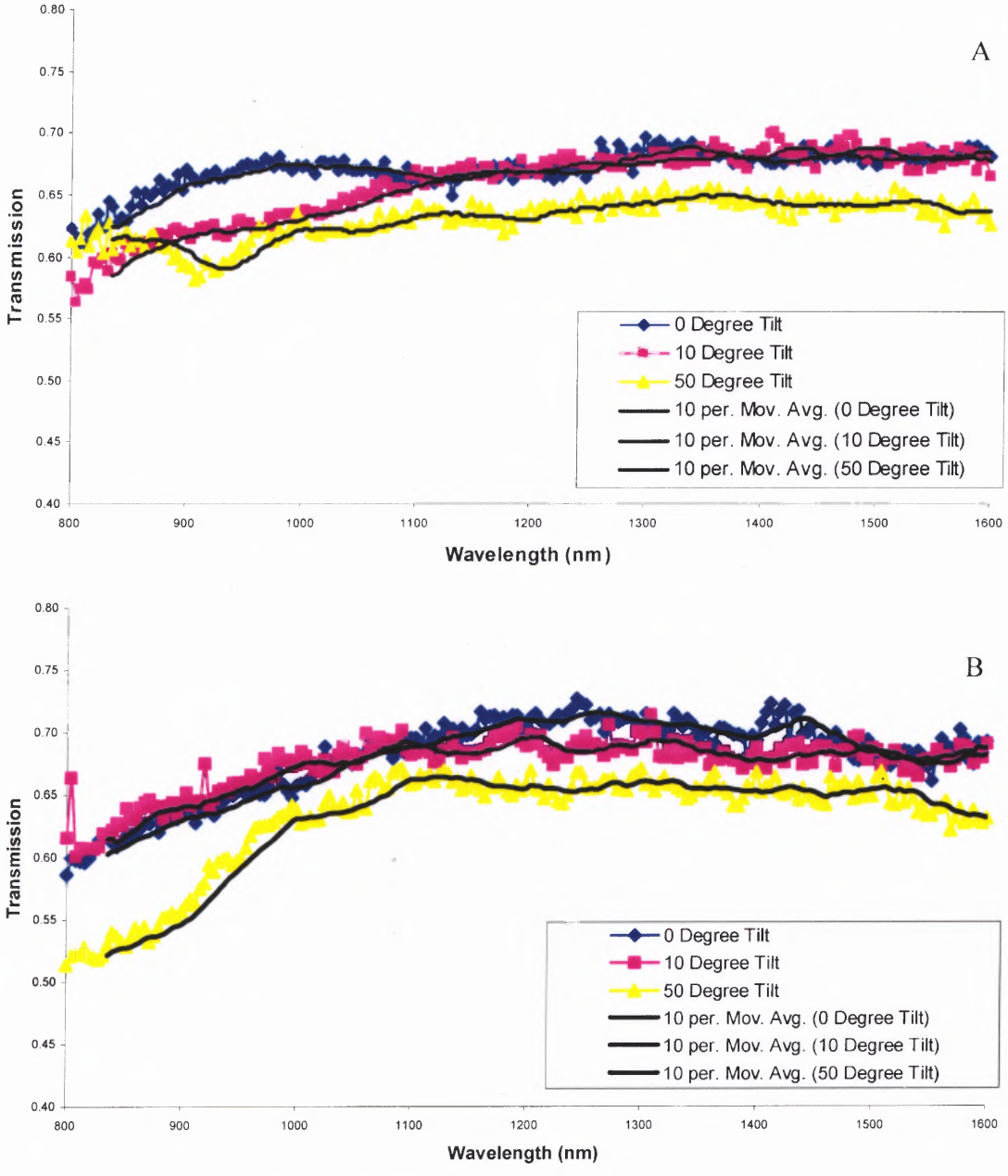

Figure 4.27 White light transmission spectra for 800 to 1600 nm wavelength. A: Parallel polarization. B: Perpendicular polarization.

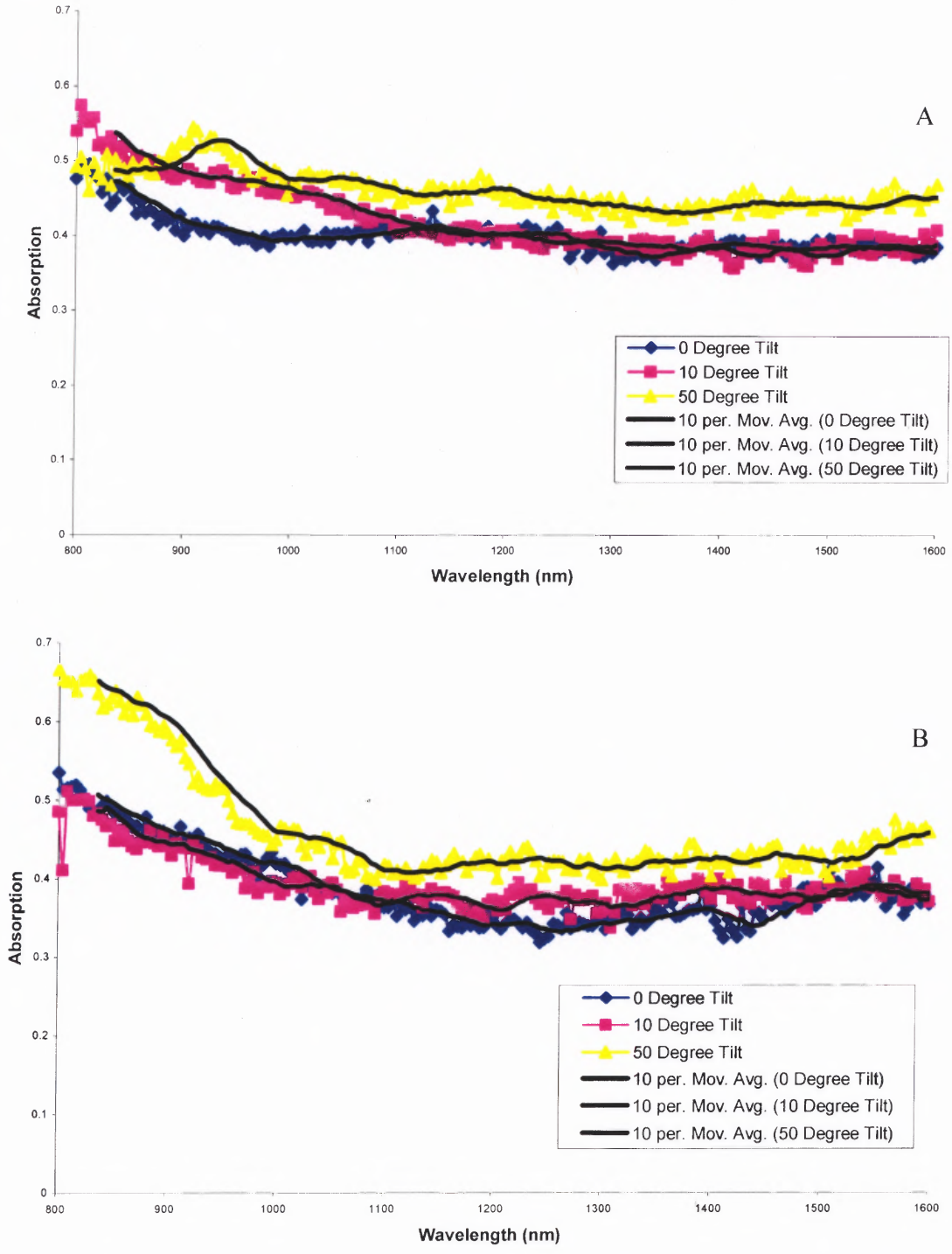

Figure 4.28 White light absorption spectra for 800 to 1600 nm wavelength. A: Parallel polarization. B: Perpendicular polarization.

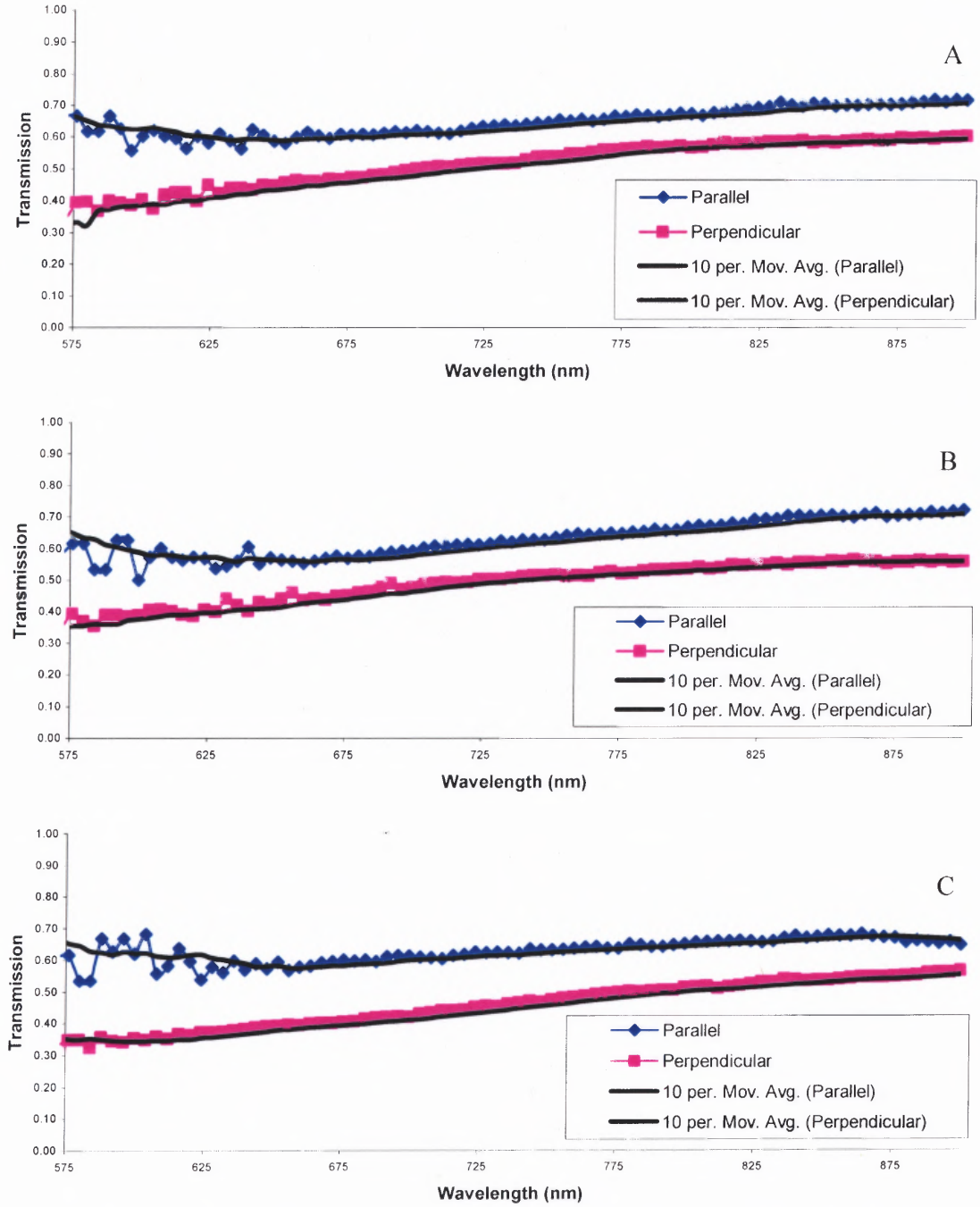

Figure 4.29 White light transmission spectra for 500 to 900 nm wavelength. A: $\theta = 0°$. B: $\theta = 10°$. C: $\theta = 50°$.

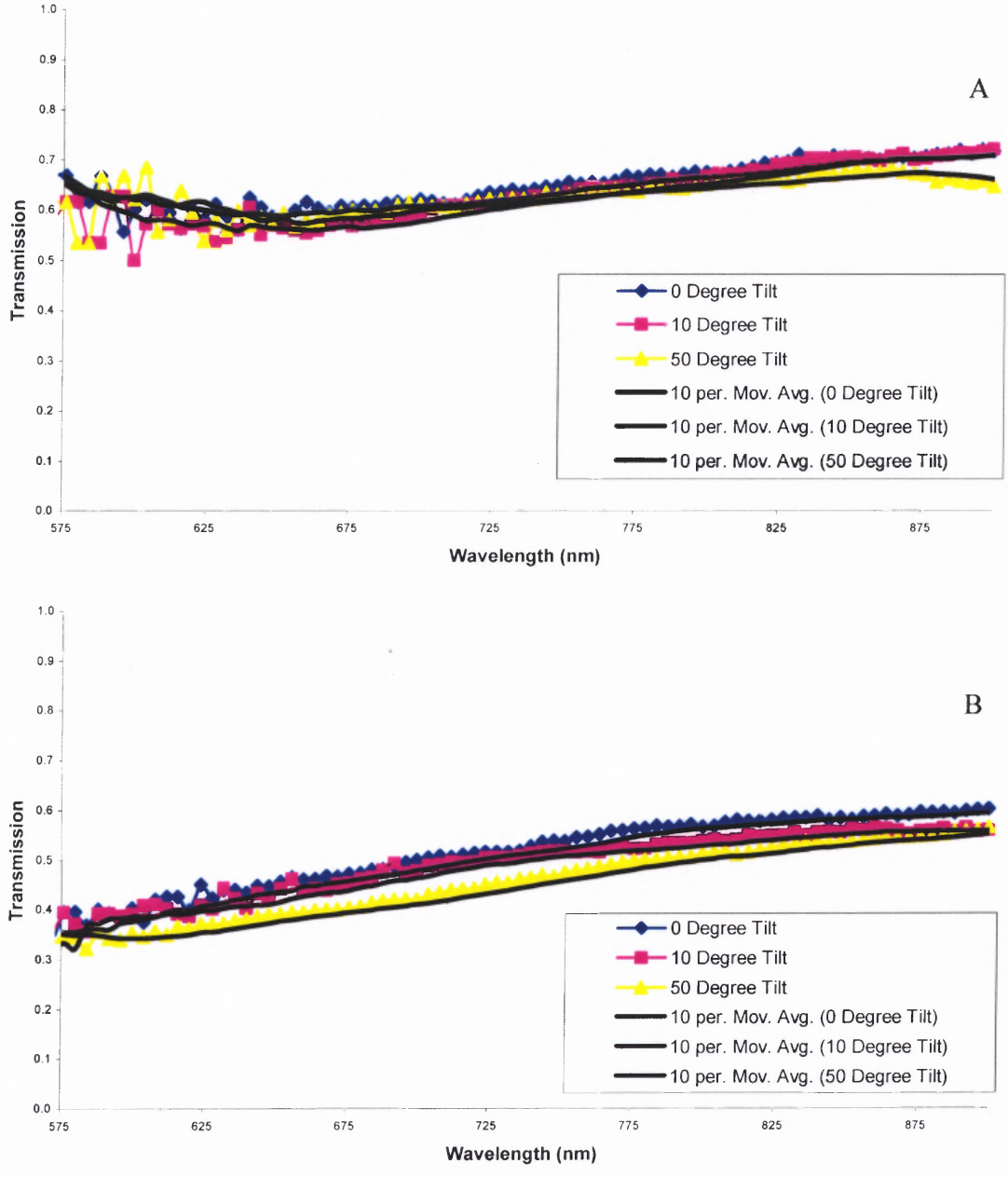

Figure 4.30 White light transmission spectra for 575 to 900 nm wavelength. A: Parallel polarization. B: Perpendicular polarization.

In Figure 4.31 the absorption was calculated as A = -lnT where A is the absorption and T is the transmission.

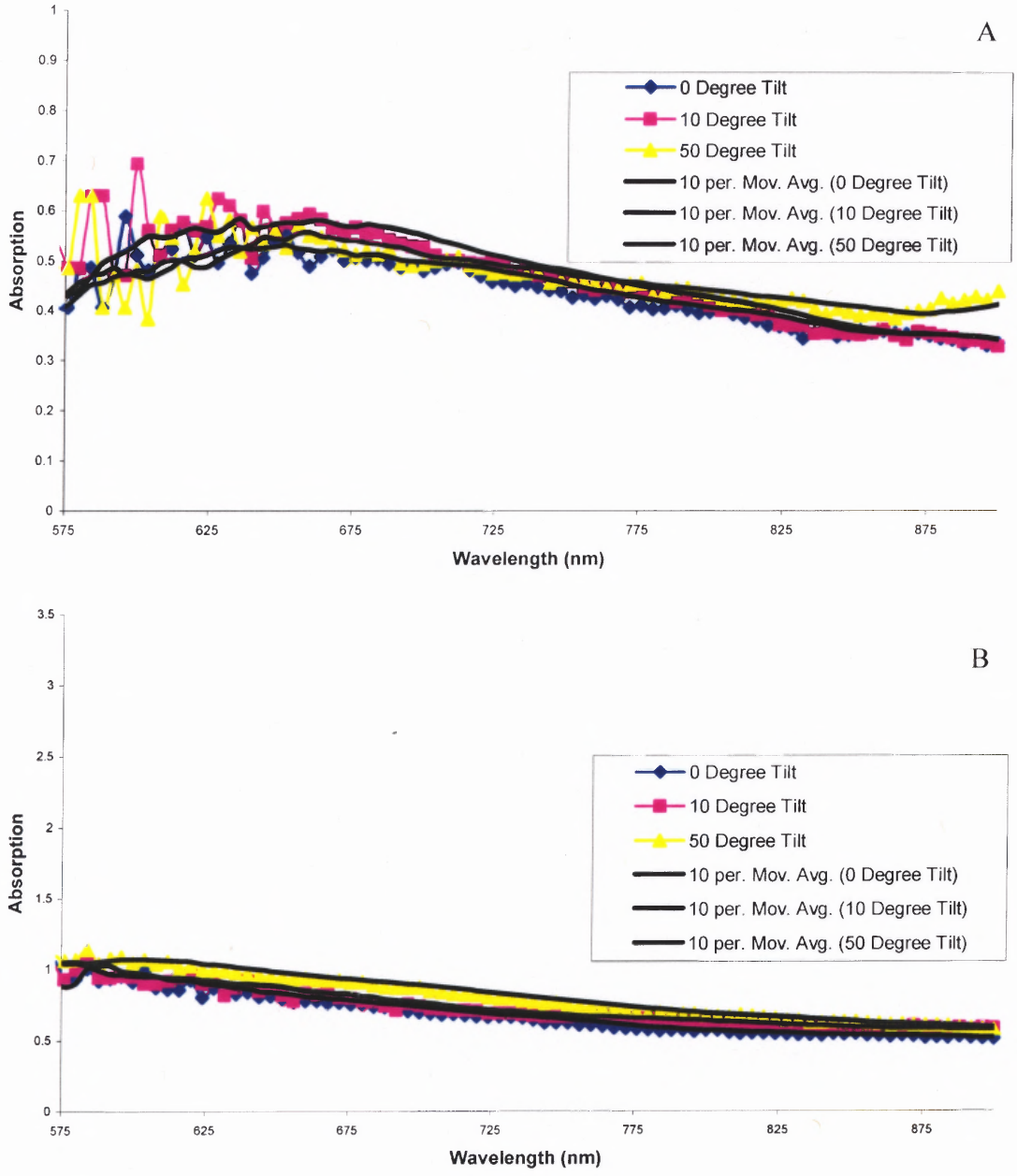

Figure 4.31 White light absorption spectra for 500 to 900 nm wavelength. A: Parallel polarization. B: Perpendicular polarization.

A 1200 lines/mm grating was used for Figures 4.32 – 4.34. The 1200 lines/mm grating limits the spectrum up to 750 nm but it allows the spectrum to reach down to 400 nm which is the limit for the detector. The spectra were cut off at 450 nm for perpendicular polarization because the noise level was too great below 450 nm.

Figure 4.32 compares the spectra for parallel polarization and perpendicular polarization for each angle for 450 to 750 nm wavelength.

Figure 4.33 shows that the transmission spectra for perpendicularly or parallel polarized light does not change with incidence angle. Although this is unexpected, it agrees with the results from Figure 4.30.

The absorption was calculated in Figure 4.34 as $A = -\ln T$ where A is the absorption and T is the transmission.

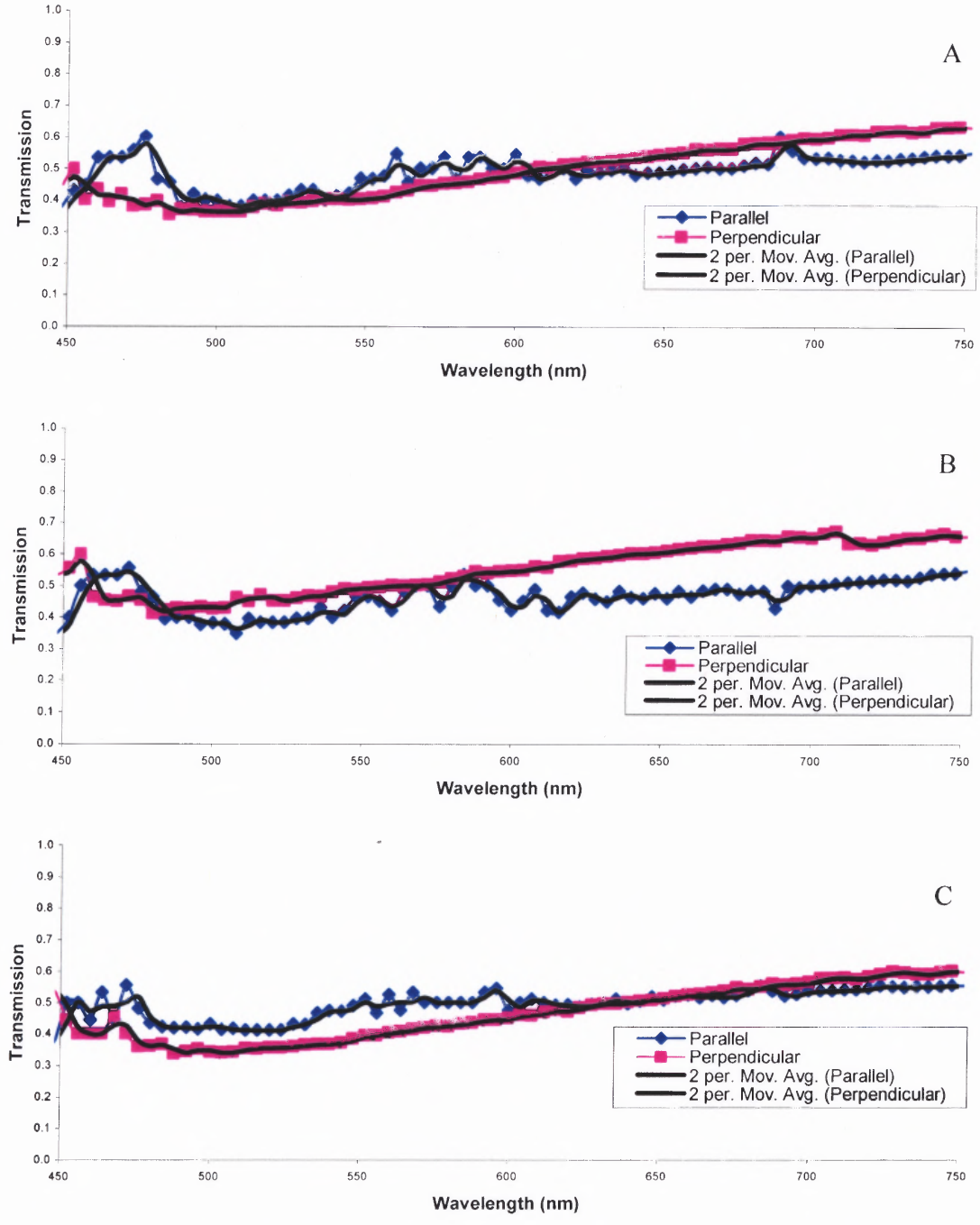

Figure 4.32 White light transmission spectra for 450 to 750 nm wavelength. A: $\theta = 0°$. B: $\theta = 10°$. C: $\theta = 50°$

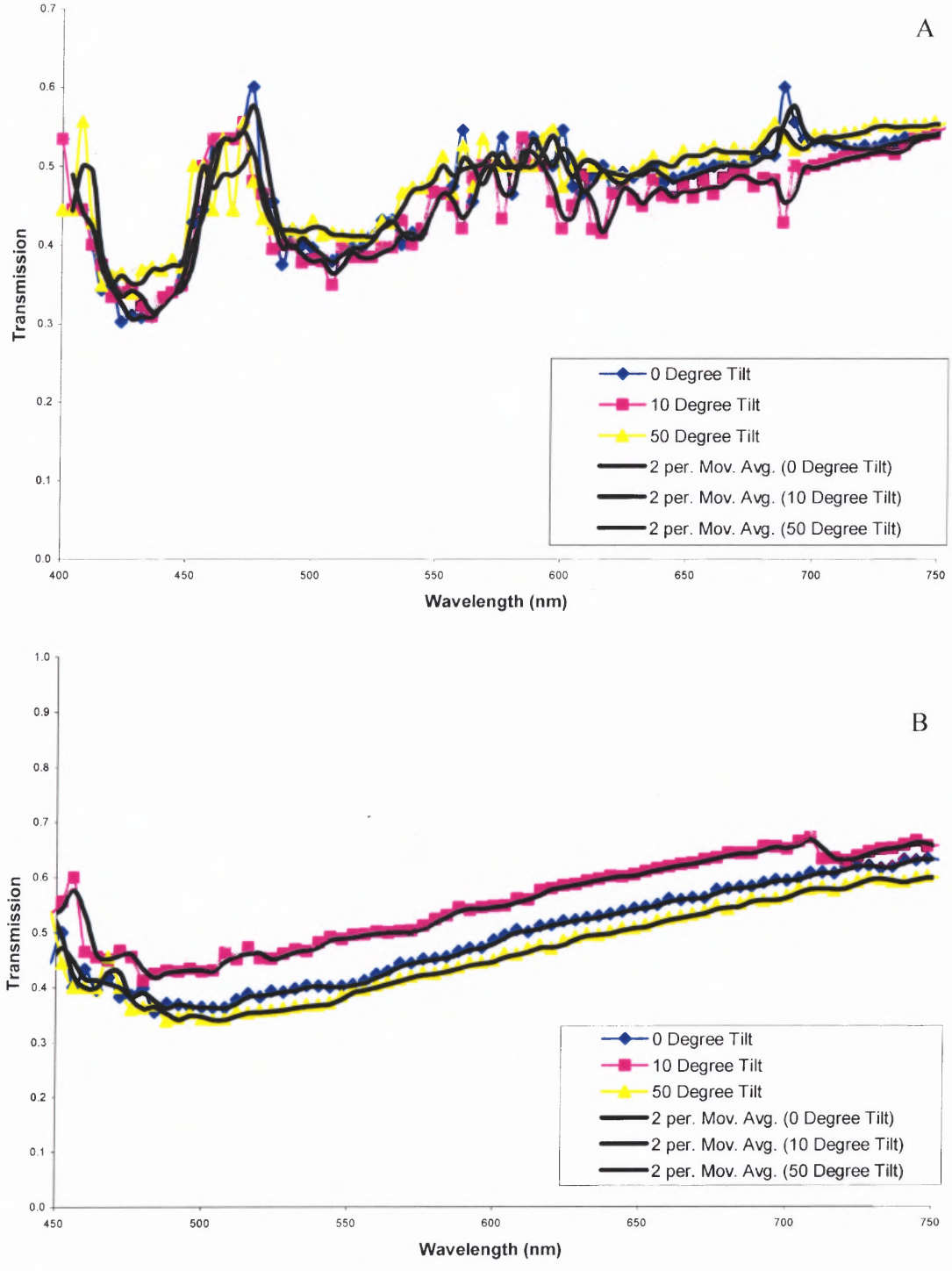

Figure 4.33 White light transmission spectra for A: Parallel polarization. 400 to 750 nm wavelength. B: Perpendicular polarization. 450 to 750 nm wavelength.

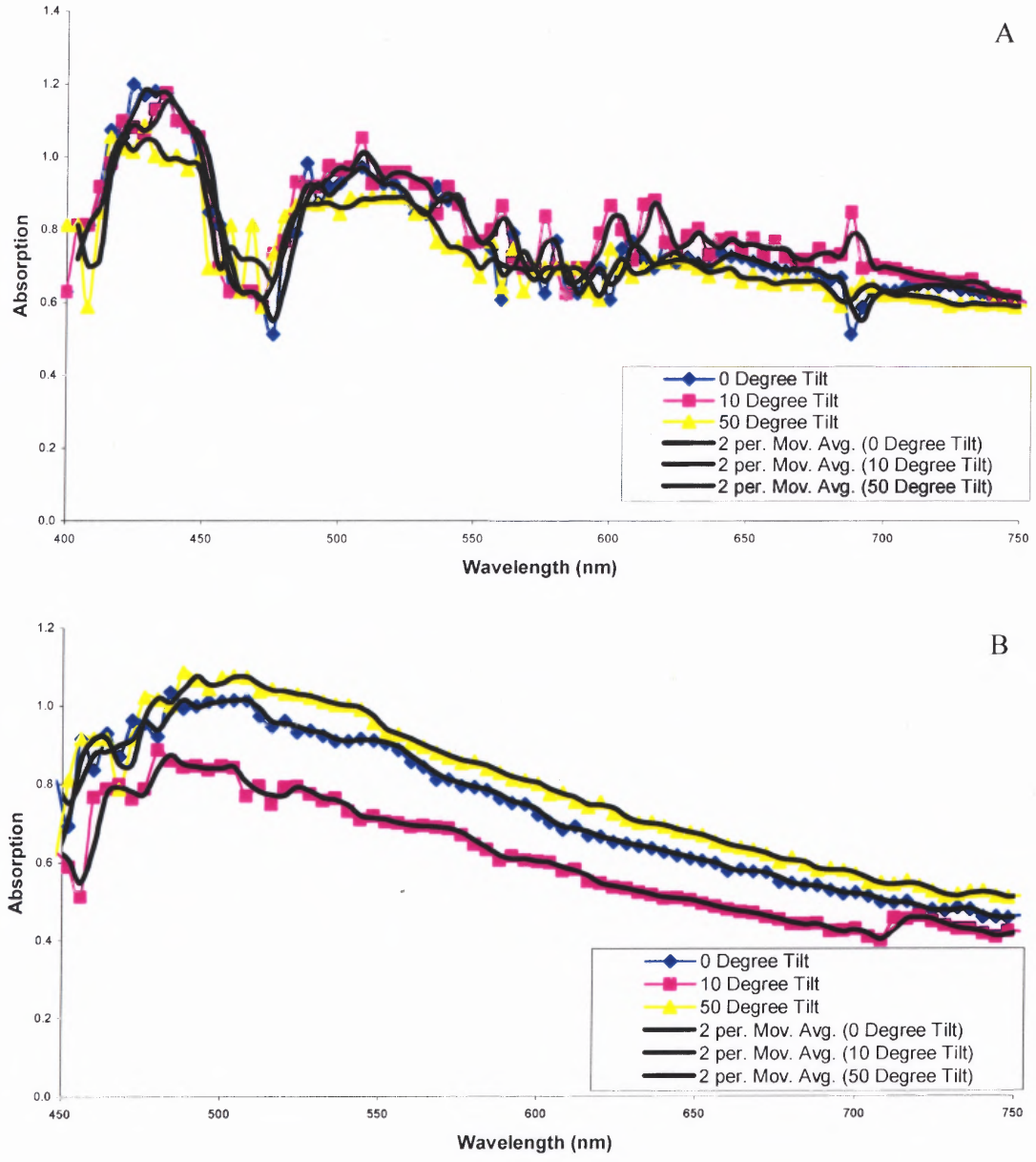

Figure 4.34 White light absorption spectra for A: Parallel polarization. 400 to 750 nm wavelength. B: Perpendicular polarization. 450 to 750 nm wavelength.

CHAPTER 5

SUMMARY

5.1 Conclusions

The new pulsed laser ablation has been assembled and tested. It successfully produced hexagonal Si droplets up to 49 μm in diameter. The general performance has been improved in comparison with the system previously used in the laboratory. The new system has the ability to control many parameters. Target-substrate separation, which was fixed in the previous system, is now adjustable. The target in the previous system was stationary requiring the laser beam to be rastered during deposition to avoid drilling through the target while the target in the new system can rotate during deposition allowing the laser beam focal point to remain stationary. If position of the laser beam focal point has an effect on deposition, this new configuration is desirable. The large observation window in the new system makes aiming the laser onto the target easier compared to the previous system which only had a window for the laser beam. The increased target size and capability to hold many samples greatly improves the efficiency of performing experiments. The previous system could only hold one sample and a small target. The vacuum that can be achieved with the new system is 2.2×10^{-7} Torr compared to 10^{-6} Torr for the previous system.

With the improved system, the effects of the variation of the controllable parameters on hexagonal Si formation were investigated. The varied parameters included: lens arrangement, target rotation, laser pulse power, laser pulse frequency, deposition time, number of pulses, target-substrate separation, and target heating.

The maximum droplet diameter and the number of larger droplets were considered the indicators of the optimum lens arrangement. The results were clear that using the 15 cm focal length lens as the laser focusing lens yielded larger droplets than obtained with 10 cm focal length lens. A rotating target consistently yielded fewer and smaller droplets than a still target. Higher laser pulse power consistently created the largest droplet diameter. Laser pulse frequency does not clearly affect droplet size, however it does affect the total droplet count, which increases with increasing laser pulse frequency.

The maximum droplet diameter, up to 33 μm, increases proportionally with increasing deposition time, up to 8 minutes. This is interpreted as due to the inverse relationship between the droplet size and the probability of its appearance, in this size range. Thus a longer time is required to find a larger droplet. A similar effect was observed by varying the number of pulses. For three sets of pulses (10, 100, and 1000), the maximum droplet diameter increased with increasing number of pulses.

Target-substrate separation does not have a significant effect on the maximum droplet diameter. There is however an indication that the number of larger droplets ($\geq$ 5 μm) increases with increasing distance. This effect should be investigated further because of its significance to the understanding of the mechanism of the hexagonal crystallite formation. Larger target-substrate distance corresponds to a longer residence time of the effluent in the vacuum, where the droplets may be formed.

Target heating did not have a consistent effect on droplet size or droplet count. This may have been due to insufficient heating by the sources. The maximum temperature either source can achieve in air is ~200°C. Even if the temperature increase

is larger in vacuum, it may not be significant when compared to the 1414°C melting point of Si.

Characterization of the deposited samples allowed for greater understanding of the structure of the droplets. Raman spectroscopy showed that the PLA system used for this thesis successfully produces hexagonal Si. The peaks in measured spectra had the appropriate Raman shift for hexagonal Si. Some samples did not exhibit peaks at all, but this was due to the Raman system's inability to aim its laser directly on a droplet. Scanning electron microscopy helped in understanding the three dimensional structure of the droplets. An interesting question for further study is whether there is a significant difference in the structure and properties of the conical crystallites and the crater shaped droplets.

The white light transmission spectra in the 800 – 1600 nm range exhibited an expected change with angle for parallel polarized light and no change with angle for perpendicularly polarized light, which was also expected. In the 400 – 900 nm range, the spectra unexpectedly remained unchanged with angle for parallel and perpendicularly polarized light. The lower wavelengths of the 400 – 900 nm range were cut off for both 600 lines/mm and 1200 lines/mm gratings due to low signal to noise ratio. It is possible that the expected changes were in the cut off regions.

5.2 Future Work

There were numerous problems encountered that will need to be resolved for further study.

In many cases, the droplet counts were too low for acceptable statistical error. For more effective statistical analysis, more counts could be obtained by summing the

counts of several images. To be practical, this would require computer vision to automatically count and sort the droplets by size.

Aiming of the laser beam focal point was done manually, and it was difficult to aim the focal point directly across from deposition aperture. The effect of a position on the substrate relative to the position of the laser spot on the target needs to be understood. Previous studies showed concentric rings with different properties on deposited films [9]. The effect could be studied using a larger substrate and a larger deposition aperture. If there is an effect, some method must be devised to better control the location of the spot on the target. Also, one would like to control the depth of the focal point during deposition and be able to focus on the surface of the target as it is worn deeper.

As ablation goes on, the target surface is changed as the laser beam drills deeper. It may be desirable to study the effect of surface roughness on droplet formation.

A major problem is that it is not known how much the power attenuates with time (or number of pulses) due to deposition on laser window shield. One cannot really compare the samples on a single platter since they were all deposited under different laser beam intensity, because of this effect. Also, one cannot compare the samples on different platters unless the deposition conditions for the laser window shield were the same for corresponding samples. Some method for measuring the power inside the chamber between the laser window shield and target would be desirable.

It has not been proven that heating has no effect, and a better heat source would be useful for further study. A temperature monitor for the target would also be helpful to study the effectiveness of a particular heat source.

Laser pulse power has been shown to effect droplet size. Since the maximum power for the laser used in this thesis was already studied, a more powerful laser could be used to study the effect of even higher power.

APPENDIX

EXPERIMENTAL DATA

The following tables contain the experimental parameters for each sample and the resultant droplet counts.

Table A.1 Experimental Parameters.

Sample Name	Pressure (Torr)	Deposition Time	Rotation	Laser Frequency (Hz)	Laser Pulse Power (kV)	Heating	Separation (mm)
Old System 01	NA	10min	N	20	24	N	NA
New System	NA	10min	Y	20	24	N	NA
New System (clear stripe across sample)	NA	10min	Y	20	24	N	NA
09-23-02 Rotating	3.0*10^-6	10min	Y	20	24	N	NA
09-23-02 Still	3.0*10^-6	10min	N	20	24	N	NA
09-24-02 Rotating	2.2*10^-7	10min	Y	20	24	N	NA
09-24-02 Still	2.2*10^-7	10min	N	20	24	N	NA
09-25-02 Rotating 20Hz	4.0*10^-7	10min	Y	20	24	N	NA
09-25-02 Still 20Hz	3.0*10^-7	10min	N	20	24	N	NA
09-25-02 Rotating 40Hz	4.0*10^-7	10min	Y	40	24	N	NA
09-25-02 Still 40Hz	3.0*10^-7	10min	N	40	24	N	NA
09-26-02 Still New Lens	4.5*10^-7	10min	N	20	24 24	N	NA
10-23-02 Sample 1	4.2*10^-7	10min	N	20	24	N	23.6
10-23-02 Sample 2	4.2*10^-7	10min	N	20	24	N	25.4
10-23-02 Sample 3	4.2*10^-7	10min	N	20	24	N	27.2
10-23-02 Sample 4	4.2*10^-7	10min	N	20	24	N	29.0
10-23-02 Sample 5	4.2*10^-7	10min	N	20	24	N	30.8
11-07-02 Sample 1	5.0*10^-7	10min	N	20	24	Y	24.3
11-07-02 Sample 2	5.0*10^-7	10min	N	40	24	Y	24.3
11-07-02 Sample 3	5.0*10^-7	10min	N	20	24	Y	21.3
11-07-02 Sample 4	5.0*10^-7	10min	N	40	24	Y	21.3
11-07-02 Sample 5	5.0*10^-7	10min	N	40	24	Y	18.3
notes:arc lamp heating with 30cm lens							
02-12-03 Sample 1	5.0*10^-7	10min	N	20	24	Y	24.3
02-12-03 Sample 2	5.0*10^-7	10min	N	20	24	Y	23.1
02-12-03 Sample 3	5.0*10^-7	10min	N	20	24	Y	21.9
02-12-03 Sample 4	5.0*10^-7	10min	N	20	24	Y	20.7
notes:arc lamp heating with 30cm lens							
02-21-03 Sample 1	5.0*10^-7	10min	N	20	24	N	24.3
02-21-03 Sample 2	5.0*10^-7	10min	N	20	24	N	23.1
02-21-03 Sample 3	5.0*10^-7	10min	N	20	24	N	21.9
02-21-03 Sample 4	5.0*10^-7	10min	N	20	24	N	20.7
02-21-03 Sample 5	5.0*10^-7	10min	N	20	24	N	19.5
03-07-03 Sample 1	5.0*10^-7	10min	Y	20	24	N	24.3
03-07-03 Sample 2	5.0*10^-7	10min	Y	20	24	N	23.1
03-07-03 Sample 3	5.0*10^-7	10min	Y	20	24	N	21.9
03-07-03 Sample 4	5.0*10^-7	10min	Y	20	24	N	20.7
03-07-03 Sample 5	5.0*10^-7	10min	Y	20	24	N	19.5
03-07-03 Sample 6	5.0*10^-7	10min	Y	20	24	N	18.3
03-14-03 Sample 1	5.0*10^-7	10min	Y	10	24	N	NA
03-14-03 Sample 2	5.0*10^-7	10min	Y	15	24	N	NA
03-14-03 Sample 3	5.0*10^-7	10min	Y	20	24	N	NA
03-14-03 Sample 4	5.0*10^-7	10min	Y	25	24	N	NA
03-14-03 Sample 5	5.0*10^-7	10min	Y	30	24	N	NA
03-14-03 Sample 6	5.0*10^-7	10min	Y	35	24	N	NA
03-21-03 Sample 1	5.0*10^-7	30s	Y	20	24	N	NA
03-21-03 Sample 2	5.0*10^-7	1min	Y	20	24	N	NA
03-21-03 Sample 3	5.0*10^-7	2min	Y	20	24	N	NA
03-21-03 Sample 4	5.0*10^-7	4min	Y	20	24	N	NA
03-21-03 Sample 5	5.0*10^-7	6min	Y	20	24	N	NA
03-21-03 Sample 6	5.0*10^-7	8min	Y	20	24	N	NA
03-28-03 Sample 1	5.0*10^-7	4min	Y	20	24	Y	35.0
03-28-03 Sample 2	5.0*10^-7	6min	Y	20	24	Y	35.0
03-28-03 Sample 3	5.0*10^-7	8min	Y	20	24	Y	35.0
03-28-03 Sample 4	5.0*10^-7	10min	Y	20	24	Y	35.0
03-28-03 Sample 5	5.0*10^-7	12min	Y	20	24	Y	35.0
03-28-03 Sample 6	5.0*10^-7	14min	Y	20	24	Y	35.0
notes:600W lamp heating entire target							
04-04-03 Sample 1	3.5*10^-7	10s	N	1	24	N	35.0
04-04-03 Sample 2	3.5*10^-7	10s	N	10	24	N	35.0
04-04-03 Sample 3	3.5*10^-7	100s	N	10	24	N	35.0
04-04-03 Sample 4	3.5*10^-7	10s	N	1	20	N	35.0
04-04-03 Sample 5	3.5*10^-7	10s	N	10	20	N	35.0
04-04-03 Sample 6	3.5*10^-7	100s	N	10	20	N	35.0
04-11-03 Sample 1	3.5*10^-7	100s	N	10	24	N	35.0
04-11-03 Sample 2	3.5*10^-7	100s	N	10	17	N	35.0
04-11-03 Sample 3	3.5*10^-7	100s	N	10	24	N	32.6
04-11-03 Sample 4	3.5*10^-7	100s	N	10	17	N	32.6
04-11-03 Sample 5	3.5*10^-7	100s	N	10	24	N	30.2
04-11-03 Sample 6	3.5*10^-7	100s	N	10	17	N	30.2
04-22-03 Sample 1	3.1*10^-7	10s	N	1	24	Y	35.0
04-22-03 Sample 2	3.1*10^-7	10s	N	10	24	Y	35.0
04-22-03 Sample 3	3.1*10^-7	100s	N	10	24	Y	35.0
04-22-03 Sample 4	3.1*10^-7	10s	N	10	20	Y	35.0
04-22-03 Sample 5	3.1*10^-7	100s	N	10	20	Y	35.0
04-22-03 Sample 6 (THICK)	3.1*10^-7	20min	N	10	24	Y	35.0
notes:600W lamp heating with 30cm lens							

Table A.2 Droplet Count.

Sample Name	Droplet Count																																																
Droplet size (micrometers)	1	2	3	4	5	6	7	8	9	10	11	12	13	14	15	16	17	18	19	20	21	22	23	24	25	26	27	28	29	30	31	32	33	34	35	36	37	38	39	40	41	42	43	44	45	46	47	48	49
Old System 01	160	50	20	17	20	6	6	4	5	2	3	1	2	2	0	0	0	0	0	0	0	0	0	0	0	0	0	0	0	0	0	0	0	0	0	0	0	0	0	0	0	0	0	0	0	0	0	0	0
New System	197	51	32	26	22	14	10	6	2	2	2	3	0	0	0	2	0	0	0	0	0	0	0	0	0	0	0	0	0	0	0	0	0	0	0	0	0	0	0	0	0	0	0	0	0	0	0	0	0
New System (clear stripe across sample)	224	60	43	32	20	13	9	3	3	4	3	1	2	0	0	1	0	0	0	0	0	0	0	0	0	0	0	0	0	0	0	0	0	0	0	0	0	0	0	0	0	0	0	0	0	0	0	0	0
09-23-02 Rotating	157	18	12	6	3	2	2	1	1	0	1	0	0	0	0	0	0	0	0	0	0	0	0	0	0	0	0	0	0	0	0	0	0	0	0	0	0	0	0	0	0	0	0	0	0	0	0	0	0
09-23-02 Still	119	20	28	19	16	5	4	4	7	4	1	1	2	1	2	2	0	0	0	0	0	1	0	0	0	0	0	0	0	0	0	0	0	0	0	0	0	0	0	0	0	0	0	0	0	0	0	0	0
09-24-02 Rotating	46	5	3	4	1	1	2	1	1	0	0	0	0	0	0	0	0	0	0	0	0	0	0	0	0	0	0	0	0	0	0	0	0	0	0	0	0	0	0	0	0	0	0	0	0	0	0	0	0
09-24-02 Still	111	25	18	9	3	2	3	2	2	0	1	0	3	0	0	0	0	0	0	0	0	0	0	0	0	0	0	0	0	0	0	0	0	0	0	0	0	0	0	0	0	0	0	0	0	0	0	0	0
09-25-02 Rotating 20Hz	44	2	3	1	2	0	0	0	1	0	0	0	0	0	0	0	0	0	0	0	0	0	0	0	0	0	0	0	0	0	0	0	0	0	0	0	0	0	0	0	0	0	0	0	0	0	0	0	0
09-25-02 Still 20Hz	224	53	37	28	14	6	3	2	1	2	1	0	0	2	0	0	0	0	0	0	0	0	0	0	0	0	0	0	0	0	0	0	0	0	0	0	0	0	0	0	0	0	0	0	0	0	0	0	0
09-25-02 Rotating 40Hz	118	32	21	13	4	0	2	0	0	0	0	0	0	0	0	0	0	0	0	0	0	0	0	0	0	0	0	0	0	0	0	0	0	0	0	0	0	0	0	0	0	0	0	0	0	0	0	0	0
09-25-02 Still 40Hz	96	16	17	10	8	3	1	0	2	1	0	0	0	0	0	0	0	0	0	0	0	0	0	0	0	0	0	0	0	0	0	0	0	0	0	0	0	0	0	0	0	0	0	0	0	0	0	0	0
09-26-02 Still New Lens	270	72	37	26	23	14	12	5	2	5	4	1	1	2	0	1	0	0	0	0	0	0	1	0	0	0	0	0	0	0	0	0	0	0	0	0	0	0	0	0	0	0	0	0	0	0	0	0	0
10-23-02 Sample 1	325	87	41	16	15	11	6	6	3	1	0	0	0	1	0	0	1	0	0	0	0	0	0	0	0	0	0	0	0	0	0	0	0	0	0	0	0	0	0	0	0	0	0	0	0	0	0	0	0
10-23-02 Sample 2	346	104	46	34	10	6	5	2	1	1	1	1	0	0	0	0	0	0	0	0	0	0	0	0	0	0	0	0	0	0	0	0	0	0	0	0	0	0	0	0	0	0	0	0	0	0	0	0	0
10-23-02 Sample 3	248	52	25	12	2	1	1	1	1	1	1	1	1	1	0	0	0	0	0	0	0	0	0	0	0	0	0	0	0	0	0	0	0	0	0	0	0	0	0	0	0	0	0	0	0	0	0	0	0
10-23-02 Sample 4	157	35	14	15	6	0	0	0	0	0	1	0	0	0	0	0	0	0	0	0	0	0	0	0	0	0	0	0	0	0	0	0	0	0	0	0	0	0	0	0	0	0	0	0	0	0	0	0	0
10-23-02 Sample 5	158	39	14	2	2	2	1	0	0	1	0	0	1	0	0	0	0	0	0	0	0	0	0	0	0	0	0	0	0	0	0	0	0	0	0	0	0	0	0	0	0	0	0	0	0	0	0	0	0
11-07-02 Sample 1	267	78	48	24	24	16	8	7	5	3	2	0	2	1	0	0	0	0	0	0	0	1	0	0	0	0	0	0	0	0	0	0	0	0	0	0	0	0	0	0	0	0	0	0	0	0	0	0	0
11-07-02 Sample 2	186	73	35	21	25	12	8	5	2	1	4	1	1	1	1	0	1	0	1	0	0	0	0	0	0	0	0	0	0	0	0	0	0	0	0	0	0	0	0	0	0	0	0	0	0	0	0	0	0
11-07-02 Sample 3	345	92	48	28	22	14	6	4	4	2	4	0	0	1	0	0	1	0	0	1	0	0	0	0	0	0	0	0	0	0	0	0	0	0	0	0	0	0	0	0	0	0	0	0	0	0	0	0	0
11-07-02 Sample 4	269	65	55	28	24	15	7	7	3	2	1	1	2	0	0	0	0	1	0	0	0	0	0	0	0	0	0	0	0	0	0	0	0	0	0	0	0	0	0	0	0	0	0	0	0	0	0	0	0
11-07-02 Sample 5	30	1	2	1	1	2	0	0	0	0	0	0	0	0	0	0	0	0	0	0	0	0	0	0	0	0	0	0	0	0	0	0	0	0	0	0	0	0	0	0	0	0	0	0	0	0	0	0	0
02-12-03 Sample 1	84	32	26	17	11	6	2	3	4	4	0	0	0	1	2	0	0	0	0	0	0	0	0	0	0	0	0	0	0	0	0	0	0	0	0	0	0	0	0	0	0	0	0	0	0	0	0	0	0
02-12-03 Sample 2	91	75	28	31	15	9	12	2	1	1	0	2	0	0	0	0	1	0	0	0	0	0	0	0	0	0	0	0	0	0	0	0	0	0	0	0	0	0	0	0	0	0	0	0	0	0	0	0	0
02-12-03 Sample 3	123	32	31	30	12	11	4	3	0	1	3	1	1	0	0	0	0	0	0	0	1	0	0	0	0	0	0	0	0	0	0	0	0	0	0	0	0	0	0	0	0	0	0	0	0	0	0	0	0
02-12-03 Sample 4	32	23	15	5	4	3	5	2	0	0	0	0	0	0	0	0	1	0	0	0	0	0	0	0	0	0	0	0	0	0	0	0	0	0	0	0	0	0	0	0	0	0	0	0	0	0	0	0	0
02-21-03 Sample 1	173	72	34	31	13	9	5	3	3	0	0	1	3	0	0	1	0	0	0	0	0	0	0	0	0	0	0	0	0	0	0	0	0	0	0	0	0	0	0	0	0	0	0	0	0	0	0	0	0
02-21-03 Sample 2	132	55	26	16	10	5	2	3	4	1	0	0	0	0	1	0	0	0	0	0	0	0	0	0	0	0	0	0	0	0	0	0	0	0	0	0	0	0	0	0	0	0	0	0	0	0	0	0	0
02-21-03 Sample 3	122	47	28	10	13	6	2	2	0	2	1	0	0	0	0	1	0	0	0	0	0	0	0	0	0	0	0	0	0	0	0	0	0	0	0	0	0	0	0	0	0	0	0	0	0	0	0	0	0
02-21-03 Sample 4	164	61	33	21	8	7	0	4	1	1	1	1	0	0	0	0	0	2	0	0	0	0	0	0	0	0	0	0	0	0	0	0	0	0	0	0	0	0	0	0	0	0	0	0	0	0	0	0	0
02-21-03 Sample 5	40	12	4	2	1	0	0	0	0	1	0	0	0	0	0	0	0	0	0	0	0	0	0	0	0	0	0	0	0	0	0	0	0	0	0	0	0	0	0	0	0	0	0	0	0	0	0	0	0
03-07-03 Sample 1	1	4	1	1	1	1	1	0	0	0	0	0	0	0	0	0	0	0	0	0	0	0	0	0	0	0	0	0	0	0	0	0	0	0	0	0	0	0	0	0	0	0	0	0	0	0	0	0	0
03-07-03 Sample 2	2	1	0	1	1	1	0	0	0	0	0	1	0	0	0	0	0	0	0	0	0	0	0	0	0	0	0	0	0	0	0	0	0	0	0	0	0	0	0	0	0	0	0	0	0	0	0	0	0
03-07-03 Sample 3	3	0	1	0	0	0	0	0	0	0	0	0	0	0	0	0	0	0	0	0	0	0	0	0	0	0	0	0	0	0	0	0	0	0	0	0	0	0	0	0	0	0	0	0	0	0	0	0	0
03-07-03 Sample 4	12	5	3	3	5	1	0	0	0	1	0	0	0	1	0	0	0	0	0	0	0	0	0	0	0	0	0	0	0	0	0	0	0	0	0	0	0	0	0	0	0	0	0	0	0	0	0	0	0
03-07-03 Sample 5	19	3	2	0	0	0	2	0	0	0	0	0	0	0	0	1	0	0	0	0	0	0	0	0	0	0	0	0	0	0	0	0	0	0	0	0	0	0	0	0	0	0	0	0	0	0	0	0	0
03-07-03 Sample 6	13	7	1	0	2	1	0	0	0	0	1	0	0	0	0	0	0	0	0	0	0	0	0	0	0	0	0	0	0	0	0	0	0	0	0	0	0	0	0	0	0	0	0	0	0	0	0	0	0
03-14-03 Sample 1	3	1	2	0	0	0	0	0	0	0	0	0	1	0	0	0	0	0	0	0	0	0	0	0	0	0	0	0	0	0	0	0	0	0	0	0	0	0	0	0	0	0	0	0	0	0	0	0	0
03-14-03 Sample 2	5	3	2	0	1	0	1	0	0	0	1	0	0	0	0	0	0	0	0	0	0	0	0	0	0	0	0	0	0	0	0	0	0	0	0	0	0	0	0	0	0	0	0	0	0	0	0	0	0
03-14-03 Sample 3	8	3	1	0	0	1	2	0	0	0	1	0	0	0	0	0	0	0	0	0	0	0	0	0	0	0	0	0	0	0	0	0	0	0	0	0	0	0	0	0	0	0	0	0	0	0	0	0	0
03-14-03 Sample 4	6	5	6	0	2	0	0	0	0	0	0	1	0	0	0	0	0	0	0	0	0	0	0	0	0	0	0	0	0	0	0	0	0	0	0	0	0	0	0	0	0	0	0	0	0	0	0	0	0
03-14-03 Sample 5	11	3	2	0	3	0	0	0	0	0	1	0	0	0	0	0	0	0	0	0	0	0	0	0	0	0	0	0	0	0	0	0	0	0	0	0	0	0	0	0	0	0	0	0	0	0	0	0	0
03-14-03 Sample 6	14	3	4	0	1	1	2	0	1	0	0	0	0	0	0	0	0	0	0	0	0	0	0	0	0	0	0	0	0	0	0	0	0	0	0	0	0	0	0	0	0	0	0	0	0	0	0	0	0
03-21-03 Sample 1	0	0	0	0	0	0	0	0	0	0	0	0	0	0	0	0	0	0	0	0	0	0	0	0	0	0	0	0	0	0	0	0	0	0	0	0	0	0	0	0	0	0	0	0	0	0	0	0	0
03-21-03 Sample 2	7	0	2	1	1	0	0	0	0	1	0	0	0	0	0	0	0	0	0	0	0	0	0	0	0	0	0	0	0	0	0	0	0	0	0	0	0	0	0	0	0	0	0	0	0	0	0	0	0
03-21-03 Sample 3	0	0	1	0	0	0	0	0	0	0	0	0	0	0	0	0	0	0	0	0	1	0	0	0	0	0	0	0	0	0	0	0	0	0	0	0	0	0	0	0	0	0	0	0	0	0	0	0	0
03-21-03 Sample 4	6	3	1	1	0	1	0	0	0	0	0	0	0	0	0	0	1	0	0	1	0	0	0	0	0	0	0	0	0	0	0	0	0	0	0	0	0	0	0	0	0	0	0	0	0	0	0	0	0
03-21-03 Sample 5	9	2	3	3	1	2	1	0	1	0	0	0	0	0	0	0	0	0	0	0	0	0	1	0	0	0	0	0	0	0	0	0	0	0	0	0	0	0	0	0	0	0	0	0	0	0	0	0	0
03-21-03 Sample 6	3	6	4	2	2	0	1	0	0	0	0	0	0	0	0	0	0	0	0	0	0	0	0	0	0	0	0	0	0	0	0	0	1	0	0	0	0	0	0	0	0	0	0	0	0	0	0	0	0
03-28-03 Sample 1	0	0	1	3	0	0	1	0	0	0	0	0	0	0	0	0	0	0	0	0	0	0	0	0	0	0	0	0	0	0	0	0	0	0	0	0	1	0	0	0	0	0	0	0	0	0	0	0	0
03-28-03 Sample 2	12	6	3	2	3	1	3	0	0	0	0	0	1	0	0	0	0	0	0	0	0	0	0	0	0	1	0	0	0	0	0	0	0	0	0	0	0	0	0	0	0	0	0	0	0	0	0	0	0
03-28-03 Sample 3	18	13	10	4	5	3	0	0	0	1	1	0	0	1	1	0	0	0	0	1	0	0	0	0	0	0	0	0	0	0	0	0	0	0	0	0	0	0	0	0	0	0	0	0	0	0	0	0	0
03-28-03 Sample 4	39	17	8	6	1	1	1	0	0	0	0	2	0	0	0	0	1	0	0	0	0	0	0	0	0	0	0	0	0	0	0	0	0	0	0	0	0	0	0	0	0	0	0	0	0	0	0	0	0
03-28-03 Sample 5	82	22	14	4	6	3	4	0	2	0	1	0	0	0	0	0	0	1	0	0	0	0	0	0	0	0	0	0	0	0	0	0	0	0	0	0	0	0	0	0	0	0	0	0	0	0	0	0	0
03-28-03 Sample 6	58	20	9	2	3	2	4	0	0	0	0	0	1	0	0	0	0	0	0	0	0	0	0	0	0	0	0	0	0	0	0	0	0	0	0	0	0	0	0	0	0	0	0	0	0	0	0	0	0
04-04-03 Sample 1	0	0	1	0	0	0	0	1	0	0	0	0	0	0	0	0	0	0	0	0	0	0	0	0	0	0	0	0	0	0	0	0	0	0	0	0	0	0	0	0	0	0	0	0	0	0	0	0	0
04-04-03 Sample 2	0	0	0	0	0	0	0	0	0	0	0	0	0	0	0	0	0	0	0	0	0	0	0	0	0	1	0	0	0	0	0	0	0	0	0	0	0	0	0	0	0	0	0	0	0	0	0	0	0
04-04-03 Sample 3	14	9	2	8	0	1	1	0	0	2	0	1	0	0	0	0	0	0	0	0	0	0	0	0	0	0	0	0	0	0	0	0	0	0	0	1	0	0	0	0	0	0	0	0	0	0	0	0	0
04-04-03 Sample 4	0	1	0	0	0	0	0	0	0	0	0	0	0	0	0	0	0	0	0	0	0	0	0	0	0	0	0	0	0	0	0	0	0	0	0	0	0	0	0	0	0	0	0	0	0	0	0	0	0
04-04-03 Sample 5	0	0	0	0	0	0	0	1	1	0	0	0	0	0	0	0	1	0	0	0	0	0	0	0	0	0	0	0	0	0	0	0	0	0	0	0	0	0	0	0	0	0	0	0	0	0	0	0	0
04-04-03 Sample 6	17	11	7	4	2	4	1	1	1	0	0	0	0	0	0	0	0	0	0	0	0	0	0	0	0	1	0	0	0	0	0	0	0	0	0	0	0	0	0	0	0	0	0	0	0	0	0	0	0
04-11-03 Sample 1	15	10	3	3	2	0	1	0	2	1	1	0	0	0	0	0	0	0	0	0	0	0	0	0	0	0	0	0	0	0	0	0	0	0	0	0	0	1	0	0	0	0	0	0	0	0	0	0	0
04-11-03 Sample 2	21	7	9	2	3	1	1	1	0	0	0	0	0	0	0	0	0	0	0	0	0	0	0	0	0	0	1	0	0	0	0	0	0	0	0	0	0	0	0	0	0	0	0	0	0	0	0	0	0
04-11-03 Sample 3	18	7	5	2	2	0	4	0	0	0	0	0	0	1	1	0	0	0	0	0	0	0	0	1	0	0	0	0	0	0	1	0	0	0	0	0	0	0	0	0	0	0	0	0	0	0	0	0	0
04-11-03 Sample 4	16	10	2	6	3	1	2	0	1	1	0	0	0	0	0	0	0	0	0	0	0	0	0	1	0	0	0	0	0	0	0	0	0	0	0	0	0	0	0	0	0	0	0	0	0	0	0	0	0
04-11-03 Sample 5	18	7	6	3	1	1	1	0	0	0	2	0	0	0	0	0	0	0	0	0	0	0	0	0	0	0	0	0	0	0	0	0	0	0	0	0	0	0	0	0	1	0	0	0	0	0	0	0	0
04-11-03 Sample 6	36	15	14	7	2	2	0	2	1	2	0	0	0	0	0	0	0	0	0	0	0	0	0	0	0	1	0	0	0	0	0	0	0	0	0	0	0	0	0	0	0	0	0	0	0	0	0	0	0
04-22-03 Sample 1	0	0	1	0	0	0	0	0	0	0	0	0	0	0	0	0	0	0	0	0	0	0	0	0	0	0	0	0	0	0	0	0	0	0	0	0	0	0	0	0	0	0	0	0	0	0	0	0	0
04-22-03 Sample 2	0	0	1	1	0	0	0	0	0	0	0	1	0	0	0	0	0	0	0	0	0	0	0	0	0	0	0	0	0	0	0	0	0	0	0	0	0	0	0	0	0	0	0	0	0	0	0	0	0
04-22-03 Sample 3	16	11	4	6	0	2	2	0	0	0	0	0	0	0	0	0	0	0	0	0	0	0	0	0	0	0	0	0	0	0	0	1	0	0	0	0	0	0	0	0	0	0	0	0	0	0	0	0	1
04-22-03 Sample 4	1	0	0	0	0	0	0	0	0	1	1	0	0	0	0	0	0	0	0	0	0	0	0	0	0	0	0	0	0	0	0	0	0	0	0	0	0	0	0	0	0	0	0	0	0	0	0	0	0
04-22-03 Sample 5	13	7	4	4	1	0	0	1	0	0	0	0	0	0	0	0	0	1	0	0	0	0	0	0	0	0	0	0	0	1	0	0	0	0	0	0	0	0	0	0	0	0	0	0	0	0	0	0	0
04-22-03 Sample 6 (THICK)	49	23	12	8	7	9	7	1	3	1	0	3	1	0	0	0	1	0	0	2	0	0	0	0	0	0	0	0	0	0	0	0	0	0	0	0	1	0	0	0	0	0	0	0	0	0	0	0	0

REFERENCES

1. Yoshida, T., Y. Yamada, and T. Orii. *A novel electroluminescent diode with nanocrystalline silicon quantum dots.* in *Electron Devices Meeting, 1996., International.* 1996.

2. Guha, S., et al., *Visible light emission from Si nanocrystals grown by ion implantation and subsequent annealing.* Applied Physics Letters, 1997. **70**(10): p. 1207 - 1209.

3. Tong, S., et al., *Visible electroluminescence from nanocrystallites of silicon films prepared by plasma enhanced chemical vapor deposition.* Applied Physics Letters, 1996. **69**(5): p. 596 - 598.

4. Baru, V.G., et al., *Optical properties of Si nanocrystals prepared by magnetron sputtering.* Applied Physics Letters, 1996. **69**(27): p. 4148-4150.

5. Volodin, V.A., et al., *Raman study of silicon nanocrystals formed in SiNx films by excimer laser or thermal annealing.* Applied Physics Letters, 1998. **73**(9): p. 1212 - 1214.

6. Kasper, J.S. and R.H. Wentorf Jr., *Hexagonal (Wurtzite) Silicon.* Science, New Series, 1977. **197**(4303): p. 599.

7. Besson, J.M., et al., *Electrical properties of semimetallic silicon III and semiconductive silicon IV at ambient pressure.* Physical Review Letters, 1987. **59**(4): p. 473-476.

8. Zhang, Y., et al., *Stable hexagonal-wurtzite silicon phase by laser ablation.* Applied Physics Letters, 1999. **75**(18): p. 2758 - 2760.

9. Vijayalakshmi, S., et al., *Characterization of laser ablated silicon thin films.* Thin Solid Films, 1999. **339**(1-2): p. 102-108.

10. Patrone, L., et al., *Photoluminescence of silicon nanoclusters with reduced size dispersion produced by laser ablation.* Journal Of Applied Physics, 2000. **87**(8): p. 3829 - 3837.

11. Iqbal, Z., S. Vijayalakshmi, and H. Grebel, *Microstructure and optical properties of nanostructured silicon thin films and artificial dielectrics.* Nanostructured Materials, 1999. **12**(1-4): p. 271-276.

12. Kobliska, R.J. and S.A. Solin, *Raman Spectrum of Wurtzite Silicon.* Physical Review B, 1973. **8**(8): p. 3799–3802.

13. Vijayalakshmi, S., J. Sturmann, and H. Grebel, *Linear and nonlinear properties of laser-ablated Si films in the 9.09.6-m wavelength region.* Journal of the Optical Society of America B, 1999. **16**(8): p. 1286-1291.

14. Suzuki, N., et al., *Structures and optical properties of silicon nanocrystallites prepared by pulsed-laser ablation in inert background gas.* Applied Physics Letters, 2000. **76**(11): p. 1389 - 1391.